

# Robustness of clocks to input noise

Michele Monti,<sup>1</sup> David K. Lubensky,<sup>2</sup> and Pieter Rein ten Wolde<sup>1</sup>

<sup>1</sup>*FOM Institute AMOLF, Science Park 104, 1098 XE Amsterdam, The Netherlands*

<sup>2</sup>*Department of Physics, University of Michigan, Ann Arbor, MI 48109-1040*

To estimate the time, many organisms, ranging from cyanobacteria to animals, employ a circadian clock which is based on a limit-cycle oscillator that can tick autonomously with a nearly 24h period. Yet, a limit-cycle oscillator is not essential for knowing the time, as exemplified by bacteria that possess an “hourglass”: a system that when forced by an oscillatory light input exhibits robust oscillations from which the organism can infer the time, but that in the absence of driving relaxes to a stable fixed point. Here, using models of the Kai system of cyanobacteria, we compare a limit-cycle oscillator with two hourglass models, one that without driving relaxes exponentially and one that does so in an oscillatory fashion. In the limit of low input-noise, all three systems are equally informative on time, yet in the regime of high input-noise the limit-cycle oscillator is far superior. The same behavior is found in the Stuart-Landau model, indicating that our result is universal.

PACS numbers: 87.10.Vg, 87.16.Xa, 87.18.Tt

## INTRODUCTION

Many organisms, ranging from animals, plants, insects, to even bacteria, need to know the time to synchronize their cellular and behavioral activity with the day-night rhythm. To this end, many employ a circadian clock. Circadian clocks are biochemical systems that can oscillate autonomously with a nearly 24h period, even though they are normally entrained by environmental signals to keep them in phase with the day-night cycle. While it is clear that circadian clocks which are locked to their environment make it possible to estimate the time of the day, it is far less obvious that clocks are essential for knowing the time [1, 2]. The oscillatory light input could also be used to drive a system which in the absence of any driving would relax to a stable fixed point rather than exhibit a limit cycle. The driving would then generate oscillations from which the organism could infer the time. It thus remains an open question what the benefits of circadian clocks are in estimating the time of the day.

This question is highlighted by the timekeeping mechanisms of prokaryotes. While circadian clocks are ubiquitous in eukaryotes, the only known prokaryotes to possess circadian clocks are cyanobacteria, which exhibit photosynthesis. The most studied and best characterized circadian clock is that of the cyanobacterium *Synechococcus elongatus*, which consists of three proteins, KaiA, KaiB, and KaiC [3]. The central clock component is KaiC, which forms a hexamer that is phosphorylated and dephosphorylated in a cyclical fashion under the influence of KaiA and KaiB. In a landmark study, Kondo and coworkers managed to reconstitute this protein phosphorylation cycle in the test tube, demonstrating that this Kai system forms a bonafide circadian clock that can tick autonomously in the absence of any oscillatory driving with a period of nearly 24 hours [4]. However, *S. elongatus* is not the only cyanobacterial species. Another species is *Prochlorococcus*, which possesses *kaiB*

and *kaiC*, but lacks (functional) KaiA. Interestingly, this species exhibits daily rhythms in gene expression under light-dark (LD) cycles but no sustained circadian rhythms in constant conditions [5, 6]. Recently, Johnson and coworkers made similar observations for the purple bacterium *Rhodospseudomonas palustris*, which is unrelated to cyanobacteria but harbors homologs of KaiB and KaiC. Its growth rate depends on the KaiC homolog in LD conditions but not constant conditions [2], strongly suggesting that the bacterium uses the (homologous) Kai system to keep time. Moreover, this species too does not exhibit sustained rhythms in constant conditions, but does show daily rhythms in e.g. nitrogen fixation in cyclic conditions. *Prochlorococcus* and *R. palustris* thus appear to keep time via an “hourglass” mechanism that relies on oscillatory driving [2, 5, 6]. These observations raise the question why some bacterial species like *S. elongatus* have evolved a bonafide clock that can run freely, while other species like *Prochlorococcus* and *R. palustris* have evolved an hourglass time-keeping system.

The question under what conditions do circadian clocks evolve was addressed by Troein *et al.* using computer simulations [7]. They used an evolutionary algorithm to evolve *in silico* biochemical networks that exhibit oscillations. They found that only in the presence of seasonal variations *and* stochastic fluctuations in the input signal, systems evolved that can also oscillate autonomously. However, they did not systematically study how the performance of the different network designs depended on these variations in the input signal. Moreover, as Johnson *et al.* pointed out [2], organisms near the equator have evolved self-sustained oscillations, showing that seasonal variations cannot be essential for the evolution of bonafide clocks.

Here, we hypothesize that the optimal design of the readout system that maximizes the reliability by which cells can estimate the time depends on the noise in the input signal. To test this idea, we study three different net-

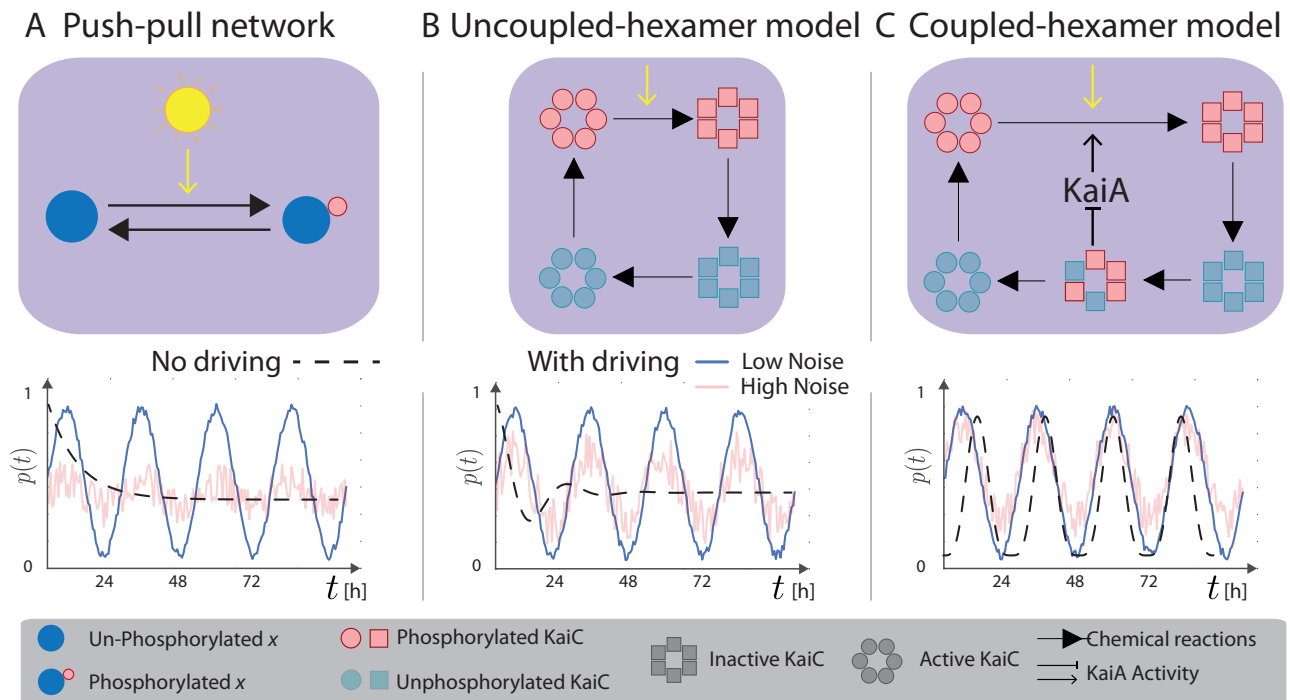


FIG. 1: Overview of different timekeeping systems. (A) A push-pull network (PPN). Each protein can switch between a phosphorylated state and an unphosphorylated one, and the input signal enhances the rate of phosphorylation. In the absence of any driving, the PPN relaxes exponentially to a steady state (middle panel). Yet, in the presence of an oscillatory input, the system exhibits oscillations which can be used as an internal clock from which the time can be inferred. (lower panel) (B) The uncoupled-hexamer model (UHM), inspired by the Kai system of *Prochlorococcus*. It consists of KaiC hexamers which can switch between active state in which the phosphorylation level tends to rise and an inactive one in which it tends to fall. The rate of phosphorylation is, presumably via changes in the ATP/ADP ratio, enhanced by the light input [8, 9]. The system is akin to a linear harmonic oscillator: it exhibits an intrinsic frequency  $\omega_0$ , resulting from the protein phosphorylation cycle of the hexamers. However, the hexamers are not coupled via KaiA as in the coupled-hexamer model shown in panel C, such that it cannot sustain autonomous oscillations; in the absence of any driving, it relaxes in an oscillatory fashion to a stable fixed point (middle panel). (C) The coupled-hexamer model (CHM), inspired by the Kai system of *S. elongatus*. Like the UHM, it consists of KaiC hexamers, which each tend to be phosphorylated in a cyclic fashion. However, in contrast to the UHM, the hexamers are coupled and synchronized via KaiA, such that the system can exhibit limit-cycle oscillations in the absence of any driving (middle panel). In all models, time is estimated from the fraction  $p(t)$  of phosphorylated proteins.

work designs from which the cell can infer time (Fig. 1): 1) a simple push-pull network (PPN), in which a read-out protein switches between a phosphorylated and an unphosphorylated state (Fig. 1A). Because the phosphorylation rate increases with the light intensity, the phosphorylation level oscillates in the presence of oscillatory driving, enabling the cell to estimate the time. This network lacks an intrinsic oscillation frequency, and in the absence of any driving it relaxes to a stable fixed point in an exponential fashion; 2) an uncoupled hexamer model (UHM), which is inspired by the Kai system of *Prochlorococcus* (Fig. 1B). This model consists of KaiC hexamers which each have an inherent propensity to proceed through a phosphorylation cycle. However, the phosphorylation cycles of the respective hexamers are not coupled among each other, and without a common forcing the cycles will therefore desynchronize, leading to the loss of macroscopic oscillations. In contrast to the proteins of

the PPN, each hexamer is a tiny oscillator with an intrinsic frequency  $\omega_0$ , which means that an ensemble of hexamers that has been synchronized initially, will, in the absence of driving, relax to its fixed point in an oscillatory manner. 3) coupled hexamer model (CHM), which is inspired by the Kai system of *S. elongatus* (Fig. 1C). As in the previous UHM, each hexamer has an intrinsic capacity to proceed through a phosphorylation cycle, but, in contrast to that system, the cycles of the respective hexamers are coupled and synchronized via KaiA, as described further below. Consequently, this system exhibits a limit cycle, yielding macroscopic oscillations with intrinsic frequency  $\omega_0$  even in the absence of any driving.

Here we are interested in the question how the accuracy of estimating time is limited by the noise in the input signal, and how this limit depends on the architecture of the readout network. We are therefore interested in the regime that the intrinsic noise can be ignored [10],

which means that we model the different systems using mean-field (deterministic) chemical rate equations.

The chemical rate equation of the PPN model is given by  $\dot{x}_p = k_f s(t)(x_T - x_p(t)) - k_b x_p(t)$ , where  $x_p(t)$  is the concentration of phosphorylated protein,  $x_T$  is the total concentration,  $k_f s(t)$  is the phosphorylation rate  $k_f$  times the input signal  $s(t)$ , and  $k_b$  is the dephosphorylation rate. The uncoupled (UHM) and coupled (CHM) hexamer model are based on a minimal model of the Kai system of *S. elongatus*, which in the past decade has been modeled extensively due to a wealth of data [11–18]. In both models, KaiC switches between an active conformation in which the phosphorylation level tends to rise and an inactive one in which it tends to fall [11, 16]. Experiments indicate that the principal Zeitgeber is the ATP/ADP ratio [8, 9], which means that the clock predominantly couples to the input  $s(t)$  during the phosphorylation phase of the oscillations [8, 18]. Inspired by this observation, in both the UHM and the CHM,  $s(t)$  modulates the phosphorylation rate of active KaiC. Since, in *S. elongatus*, KaiB does not directly affect the (de)phosphorylation rate but mainly plays a role in stabilizing inactive KaiC and mediating KaiA binding [11, 12, 16, 17], KaiB is not modeled explicitly. The principal difference between the UHM and CHM is KaiA: (functional) KaiA is absent in *Prochlorococcus* and hence in the UHM [5, 6]. In contrast, in *S. elongatus* and hence the CHM, KaiA phosphorylates active KaiC, yet inactive KaiC can via KaiB strongly bind KaiA too. This gives rise to the synchronisation mechanism of differential affinity [11, 12], in which inactive hexamers that are still in the dephosphorylation phase of the cycle take away KaiA from those hexamers that have already finished their cycle, thereby halting their next round of phosphorylation. In all three models, the input is modeled as a sinusoidal signal with mean  $\bar{s}$  and driving frequency  $\omega = 2\pi/T$  plus additive noise  $\eta_s(t)$ :  $s(t) = \sin(\omega t) + \bar{s} + \eta_s(t)$ . The noise is uncorrelated with the mean signal, and has strength  $\sigma_s^2$  and correlation time  $\tau_c$ ,  $\langle \eta_s(t)\eta_s(t') \rangle = \sigma_s^2 e^{-|t-t'|/\tau_c}$ . A detailed description of the different models is given in [20].

As a performance measure for the accuracy of estimating time, we use the mutual information  $I(p; t)$  between the time  $t$  and the phosphorylation level  $p(t)$  [10, 19]:

$$I(p; t) = \int_0^T dt \int_0^1 dp P(p, t) \log_2 \frac{P(p, t)}{P(p)P(t)}. \quad (1)$$

Here  $P(p, t)$  is the joint probability distribution while  $P(p)$  and  $P(t) = 1/T$  are the marginal distributions for observing  $p$  and  $t$ . The mutual information quantifies the number of distinct time points that can be inferred uniquely from the phosphorylation level  $p(t)$ . The distributions are obtained from running long simulations of the chemical rate equations of the different models [20].

For each system, we first optimized the parameters to maximize the mutual information [20]. For the PPN,

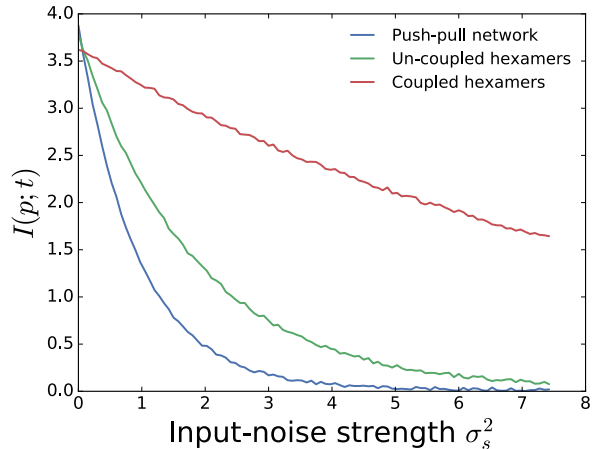


FIG. 2: The mutual information  $I(p; t)$  as a function of the input-noise strength  $\sigma_s^2$ , for the push-pull network (PPN), the uncoupled-hexamer model (UHM) and the coupled-hexamer model (CHM), see Fig. 1. In the limit of low input noise, all systems are equally informative on time, yet in the high-noise regime the CHM is most accurate. The parameters have been optimized to maximize  $I(p; t)$ ; since these are (nearly) independent of  $\sigma_s^2$ , they are fixed (see Table S1 [20]).

there exists an optimal response time  $\tau_r \sim 1/k_b$  that maximizes  $I(p; t)$ , which can be understood as a trade-off between maximizing the amplitude of  $p(t)$ , which increases with decreasing  $\tau_r$ , and minimizing the noise in  $p(t)$ , which decreases with increasing  $\tau_r$  because of time averaging [20, 21]. Similarly, for the UHM, there exists an optimal intrinsic frequency  $\omega_0$  of the individual hexamers. Because the UHM is linear, its behavior is similar to the simplest system with an intrinsic frequency, the (damped) harmonic oscillator. Analyzing this system shows that while the amplitude  $A$  of the output  $x(t)$  is maximized at resonance,  $\omega_0 \rightarrow \omega$ , the standard deviation  $\sigma_x$  of  $x$  is maximized when  $\omega_0 \rightarrow 0$ , such that the signal-to-noise ratio  $A/\sigma_x$  peaks for  $\omega_0 > \omega$  [20]. Interestingly, also the CHM exhibits a maximum in  $A/\sigma_x$  for intrinsic frequencies that are slightly off-resonance [20].

Fig. 2 shows the mutual information  $I(p; t)$  as a function of the input-noise strength  $\sigma_s^2$  for the three systems. In the limit that  $\sigma_s^2$  is small,  $I(p; t)$  is essentially the same for all systems. In this regime, they are equally informative on time. However, the figure also shows that as  $\sigma_s^2$  rises,  $I(p; t)$  of the UHM and especially the PPN decrease very rapidly, while that of the CHM falls much more slowly. In fact, for  $\sigma_s^2 \approx 3$ ,  $I(p; t)$  of the CHM is still far above 2 bits, while  $I(p; t)$  of the PPN and that of the UHM have already dropped below 1 bit, meaning that using these systems, the cell would no longer be able to distinguish between day and night. Indeed, this figure shows that in the regime of high input noise, a bonafide clock that can tick autonomously is a much better time-

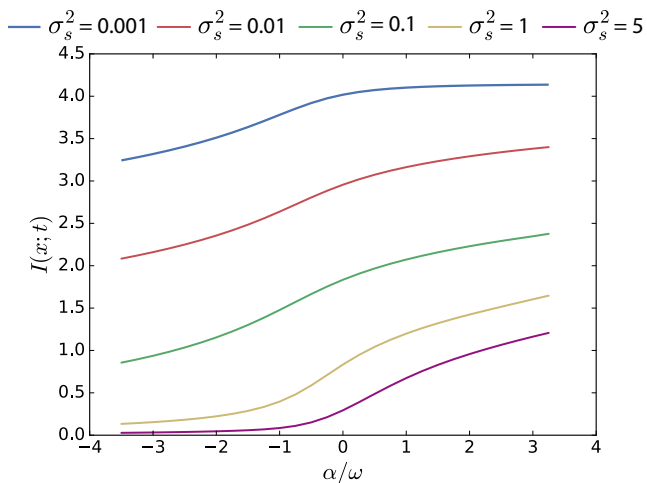


FIG. 3: The mutual information  $I(p; t)$  as a function of  $\alpha$  of the Stuart-Landau model (see Eq. 2), for different strengths of the input noise  $\sigma_s^2$ . When  $\alpha < 0$ , the system corresponds to a damped oscillator like the uncoupled-hexamer model (UHM). When  $\alpha > 0$ , the system can sustain autonomous oscillations, like the coupled-hexamer model (CHM). Clearly, the mutual information rises as the system is changed from a damped oscillator into a bonafide clock that exhibits limit-cycle oscillations. Moreover, the increase is most pronounced when the input noise is large, as also observed for the UHM and the CHM (see Fig. 2). Parameters:  $\nu = 0$ ;  $\beta = \omega$ ;  $\epsilon = 0.5\omega$ .

keeper than a system which relies on oscillatory driving for showing oscillations. This is the principal result of our paper. It is observed for other values of  $\tau_c$  and other types of input signals, such as a truncated sinusoid corresponding to no driving at night (see Fig. S4 of [20]).

The robustness of our observation that bonafide clocks are more reliable timekeepers especially when the input noise is large, suggests that it is a universal phenomenon, independent of the details of the system. We therefore analyzed a generic minimal model, the Stuart-Landau model. It allows us to study how the capacity to infer time changes as a system is altered from a damped (nearly) linear oscillator, which has a characteristic frequency but cannot sustain oscillations in the absence of driving, to a (weakly) non-linear oscillator that can sustain autonomous oscillations [20]. Near the Hopf bifurcation where a limit cycle appears the effect of the non-linearity is weak, so that the solution  $x(t)$  is close to that of a linear harmonic oscillator; this means that when the system is driven by a sinusoidal signal  $s(t)$  with frequency  $\omega(t)$ , the solution has the form  $x(t) = 1/2(A(t)e^{i\omega t} + c.c.)$ , where  $A(t)$  is a complex amplitude that can be time-dependent [22]. The dynamics of  $A(t)$  is then given by

$$\dot{A} = -i\nu A + \alpha A - \beta|A|^2 A - \epsilon E, \quad (2)$$

where  $\nu \equiv (\omega^2 - \omega_0^2)/(2\omega)$  with  $\omega_0$  the intrinsic frequency,  $\alpha$  and  $\beta$  are parameters that govern the linear and non-linear growth and decay of oscillations,  $E$  is the first har-

monic of  $s(t)$  and  $\epsilon$  describes the coupling strength [22]. Eq. 2 gives a universal description of a driven weakly non-linear oscillator near the Hopf bifurcation [22].

The non-driven system exhibits a Hopf bifurcation at  $\alpha = 0$ . This means that by varying  $\alpha$  we can change the system from a *damped oscillator* (defined by  $\alpha < 0$ ) which in the absence of driving exhibits oscillations that decay, to an *limit-cycle oscillator* ( $\alpha > 0$ ) that shows free-running oscillations. The driven damped oscillator system ( $\alpha < 0$ ) always has one stable fixed point with  $|A| > 0$  corresponding to sinusoidal oscillations that are synchronized with the driving. The driven limit-cycle oscillator system ( $\alpha > 0$ ), however, can exhibit different dynamics, ranging from perfect synchronization, where  $x(t)$  has a constant amplitude  $A$  and constant phase shift with respect to  $s(t)$ , to quasi-periodic oscillations of  $x(t)$ , arising from limit-cycle dynamics of  $A(t)$  [22]. Here we limit ourselves to perfect synchronisation.

To compute  $I(x, t)$ , we use an approach that is inspired by the linear-noise approximation for computing noise in biochemical networks, and which we have employed before in this context [10, 19]. It assumes that  $P(x|t)$  is a Gaussian distribution with variance  $\sigma_x^2(t)$  centered at the deterministic solution  $x(t) = 1/2(Ae^{i\omega t} + c.c.)$ , where  $A$  is obtained by solving Eq. 2 in steady state. To find  $\sigma_x^2$ , we first compute  $\sigma_A^2$  from Eq. 2 by adding Gaussian white-noise of strength  $\sigma_s^2$  to  $E$  and expanding  $A$  to linear order around its fixed point;  $\sigma_x^2(t)$  is then obtained from  $\sigma_A^2$  via a coordinate transformation [20].

Fig. 3 shows the mutual information  $I(x; t)$  as a function  $\alpha$ , for different values of  $\sigma_s^2$ . The figure shows that  $I(x; t)$  rises as the system is changed from a damped oscillator  $\alpha < 0$  to a self-sustained oscillator ( $\alpha > 0$ ). Moreover, the increase is most pronounced when the input noise  $\sigma_s^2$  is large. The Stuart-Landau model thus reproduces the behavior of the computational models in Fig. 2. It shows that the principal result of our study is universal: when the input noise is small, a system that shows sustained oscillations only in response to driving can keep time as reliably as a limit-cycle oscillator, which can generate oscillations autonomously; yet for high input noise, a limit-cycle oscillator is superior.

The PPN and UHM are readout systems that in the absence of driving relax to a stable fixed point. The signal generates oscillations by driving the fixed point around in state space, and noise in the input then moves the fixed point around in a stochastic fashion. While the driven system exhibits a cycle in state space, the trajectory is determined by the strength of the input, creating a trade-off between gain (amplitude) and noise that cannot be lifted [20]. The CHM is a limit-cycle oscillator, which is markedly different. In the absence of driving, it already moves around a cycle in state space with a well-defined amplitude and pace: the limit cycle. This cycle is an intrinsic and robust property of the system. While coupling the system to the input is necessary for main-

taining a stable phase relationship with the environment, weak forcing does not significantly change the trajectory of the limit cycle, making these oscillators more robust to input noise [20]. Lastly, we note that in our minimal models the formal distinction between internal and input noise vanishes—the same additive noise term could be used to model either source. This leaves open the possibility that limit-cycle oscillators are also more robust to internal noise. We leave this question for future work.

This work is part of the research programme of the Netherlands Organisation for Scientific Research (NWO) and was performed at AMOLF. DKL acknowledges NSF grant DMR 1056456 and grant PHY 1607611 to the Aspen Center for Physics, where part of this work was completed. We thank Jeroen van Zon and Nils Becker for a critical reading of the manuscript.

- 
- [1] T. Roenneberg and M. Merrow, *Journal of Biological Rhythms* **17**, 495 (2002).
- [2] P. Ma *et al.*, *PLoS genetics* **12**, e1005922 (2016).
- [3] M. Ishiura *et al.*, *Science* **281**, 1519 (1998).
- [4] M. Nakajima *et al.*, *Science (New York, N.Y.)* **308**, 414 (2005).
- [5] J. Holtzendorff *et al.*, *Journal of Biological Rhythms* **23**, 187 (2008).
- [6] E. R. Zinser *et al.*, *PLoS ONE* **4**, e5135 (2009).
- [7] C. Troein, J. C. W. Locke, M. S. Turner, and A. J. Millar, *Current Biology* **19**, 1961 (2009).
- [8] M. J. Rust, S. S. Golden, and E. K. O’Shea, *Science (New York, N.Y.)* **331**, 220 (2011).
- [9] G. K. Pattanayak, G. Lambert, K. Bernat, and M. J. Rust, *Cell Reports* **13**, 2362 (2015).
- [10] M. Monti, D. K. Lubensky, and P. R. ten Wolde, [arXiv.org:1706.02226](https://arxiv.org/abs/1706.02226) (2017).
- [11] J. S. van Zon, D. K. Lubensky, P. R. H. Altena, and P. R. ten Wolde, *Proc Natl Acad Sci USA* **104**, 7420 (2007).
- [12] M. J. Rust *et al.*, *Science* **318**, 809 (2007).
- [13] S. Clodong *et al.*, *Molecular Systems Biology* **3**, 90 (2007).
- [14] T. Mori *et al.*, *PLoS Biology* **5**, e93 (2007).
- [15] D. Zwicker, D. K. Lubensky, and P. R. ten Wolde, *Proceedings of the National Academy of Sciences of the United States of America* **107**, 22540 (2010).
- [16] J. Lin, J. Chew, U. Chockanathan, and M. J. Rust, *Proceedings of the National Academy of Sciences of the United States of America* **111**, E3937 (2014).
- [17] J. Paijmans, D. K. Lubensky, and P. R. ten Wolde, *PLoS Computational Biology* **13**, e1005415 (2017).
- [18] J. Paijmans, D. K. Lubensky, and P. R. ten Wolde, *Biophys. J.* **113**, 157 (2017).
- [19] M. Monti and P. R. ten Wolde, *Physical Biology* **13**, 1 (2016).
- [20] Supporting Information.
- [21] N. B. Becker, A. Mugler, and P. R. ten Wolde, *Physical Review Letters* **115**, 258103 (2015).
- [22] A. Pikovsky, M. Rosenblum, and J. Kurths, *Synchronization: A universal concept in nonlinear sciences* (Cambridge University Press, Cambridge, 2003).
- [23] Y. Xu, T. Mori, and C. H. Johnson, *The EMBO journal* **19**, 3349 (2000).
- [24] Y. Nakahira *et al.*, *Proceedings of the National Academy of Sciences of the United States of America* **101**, 881 (2004).
- [25] T. Nishiwaki *et al.*, *Proceedings of the National Academy of Sciences* **101**, 13927 (2004).
- [26] J. Tomita, M. Nakajima, T. Kondo, and H. Iwasaki, *Science* **307**, 251 (2005).
- [27] S. W. Teng *et al.*, *Science* **340**, 737 (2013).
- [28] J. Paijmans, M. Bosman, P. R. ten Wolde, and D. K. Lubensky, *Proceedings of the National Academy of Sciences of the United States of America* **113**, 4063 (2016).
- [29] J. Paulsson, *Nature* **427**, 415 (2004).
- [30] S. Tănase-Nicola, P. B. Warren, and P. R. ten Wolde, *Physical Review Letters* **97**, 068102 (2006).
- [31] C. C. Govern and P. R. ten Wolde, *Physical Review Letters* **113**, 258102 (2014).
- [32] R. Cheong *et al.*, *Science* **334**, 354 (2011).
- [33] F. Tostevin and P. R. ten Wolde, *Physical Review E* **81**, 061917 (2010).
- [34] J. Guckenheimer and P. J. Holmes, *Nonlinear Oscillations, Dynamical Systems, and Bifurcations of Vector Fields* (Springer, New York, ADDRESS, 1983).
- [35] V. S. Anishchenko *et al.*, *Nonlinear dynamics of chaotic and stochastic systems: tutorial and modern developments* (2007).
- [36] P. B. Warren, S. Tănase-Nicola, and P. R. ten Wolde, *The Journal of Chemical Physics* **125**, 144904 (2006).
- [37] C. W. Gardiner, *Handbook of Stochastic Methods* (Springer-Verlag, Berlin, 1985).

## SUPPORTING INFORMATION

This supporting information provides background information on the computational models and analytical models that we have studied. The computational models are described in the next section, while the analytical models are discussed in section .

### COMPUTATIONAL MODELS

In this section, we describe the three computational models that we have considered in this study: the push-pull network; the uncoupled-hexamer model; and the coupled-hexamer model. We also describe how we have modeled the input signal and how the systems are coupled to the input. Finally, we investigate the robustness of the principal results shown in Fig. 2 of the main text. In the next section, we first describe how we have modeled the input signal. In the subsequent sections, we then describe the computational models, how they are coupled to the input, and how we have set their parameters. Table I lists the values of all the parameters of all the models. In section we show that the principal findings of Fig. 2 are robust to the type of input signal and the noise correlation time.

#### Input signal

The input signal is modeled as a sinusoidal oscillation with additive noise:

$$s(t) = \sin(\omega t) + \bar{s} + \eta_s(t), \quad (3)$$

where  $\bar{s}$  is the mean input signal and  $\eta_s(t)$  describes the input noise. The noise in the input is assumed to be uncorrelated with the mean input signal  $s(t)$ . Moreover, we assume that the input noise has strength  $\sigma_s^2$  and is colored, relaxing exponentially with correlation time  $\tau_c$ :  $\langle \eta_s(t)\eta_s(t') \rangle = \sigma_s^2 e^{-|t-t'|/\tau_c}$ .

The input signal  $s(t)$  is coupled to the system by modulating the phosphorylation rate  $k_\alpha$  of the core clock protein, as we describe in detail for the respective computational models in the next sections. Here,  $k_\alpha = k_f, k_{ps}, k_i$ , depending on the computational model. As we will see, the net phosphorylation rate is given by

$$\begin{aligned} k_\alpha s(t) &= k_\alpha s(t) \\ &= k_\alpha \bar{s} + k_\alpha (\sin(\omega t) + \eta_s). \end{aligned} \quad (4)$$

This expression shows that in the presence of oscillatory driving, the mean phosphorylation rate averaged over a period is set by  $k_\alpha \bar{s}$ , while the amplitude of the oscillation in the phosphorylation rate, which sets the strength of the forcing, is given by  $k_\alpha$ . We also note that  $k_\alpha$  amplifies not only the ‘‘true’’ signal  $\sin(\omega t)$ , but also the noise

$\eta_s$ , the consequences of which will be discussed below. Lastly, the absence of any oscillatory driving is modeled by taking  $s(t) = \bar{s}$ , such that the net phosphorylation rate is then  $k_\alpha \bar{s}$ . The phosphorylation rate in the presence of stochastic driving is thus characterized by the following parameters: the mean phosphorylation rate  $k_\alpha \bar{s}$ , the amplitude of the phosphorylation-rate oscillations  $k_\alpha$ , and the noise  $\eta_s(t)$ , characterized by the noise strength  $\sigma_s^2$  and correlation time  $\tau_c$ . We will vary  $\sigma_s^2$  and  $\tau_c$  systematically, while  $\bar{s}$  and  $k_\alpha$ , together with the other system parameters, will be optimized to maximize the mutual information, as described below.

In the simulations, realisations of  $\eta_s(t)$  are generated via the Ornstein-Uhlenbeck process

$$\dot{\eta}_s = -\eta_s/\tau_c + \xi(t), \quad (6)$$

where  $\xi(t)$  is Gaussian white noise  $\langle \xi(t)\xi(t') \rangle = \langle \xi^2 \rangle \delta(t-t')$ . This generates colored noise of  $\eta_s(t)$ ,  $\langle \eta_s(t)\eta_s(t') \rangle = \sigma_s^2 e^{-|t-t'|/\tau_c}$ , where  $\sigma_s^2 = \langle \xi^2 \rangle \tau_c/2$ .

The results of Fig. 2 of the main text correspond to  $\tau_c = 0.5/\text{h}$ . However, we have tested the robustness of the results by varying the noise correlation time  $\tau_c$ . In addition, to test the robustness of our observations to changes in the shape of the input signal, we have also varied that. These tests are described in section and the results are shown in Fig. 7. Clearly, the principal result of Fig. 2 of the main text is robust to changes in both the noise correlation time  $\tau_c$  and the shape of the mean-input signal.

#### Push-pull network

The push-pull network is described by the following reaction

$$\dot{x}_p = k_f s(t)(x_T - x_p(t)) - k_b x_p(t), \quad (7)$$

where  $x_T = x + x_p$  is the total protein concentration,  $x_p$  is the concentration of phosphorylated protein,  $k_f s(t)$  is the phosphorylation rate  $k_f$  times the input signal  $s(t)$  (see Eq. 3) and  $k_b$  is the dephosphorylation rate. Fig. 4A shows a time trace of both a driven and a non-driven push-pull network.

#### Setting the parameters

The steady-state mean phosphorylation level is set by  $\bar{p} = \bar{x}_p/x_T = k_f \bar{s}/(k_f \bar{s} + k_b)$ . We anticipated, based on the analytical calculations described in section , that a key timescale is  $k_b$  and that the system should operate in the regime in which it responds linearly to changes in the mean input  $\bar{s}$ . This means that for a given  $k_b$ ,  $k_f$  and  $\bar{s}$  cannot be too large. We have chosen  $\bar{s} = 2$ , and then varied  $k_f$  and  $k_b$  to optimize the mutual information. We then verified a posteriori that the value of  $\bar{s} = 2$  indeed puts the system in the optimal linear regime.

Parameter	Description	Value
<b>Push-pull network, Eq. 7</b>		
$k_f$	Phosphorylation rate	0.01/h
$k_b$	Dephosphorylation rate (Eq. 43)	0.3/h
<b>Uncoupled-hexamer model, Eqs. 8-13</b>		
$k_f$	Phosphorylation rate	0.26/h
$k_b$	Dephosphorylation rate	0.52/h
$k_s$	Conformational switching rate	100/h
<b>Coupled-hexamer model, Eqs. 16-22</b>		
$k_{ps}$	Autophosphorylation rate	0.0125/h
$k_b$	Dephosphorylation rate	0.1875/h
$k_s$	Conformational switching rate	100/h
$K_0$	KaiA dissociation constant $C_0$	0.0001
$K_1$	KaiA dissociation constant $C_1$	0.0003
$K_2$	KaiA dissociation constant $C_2$	0.001
$K_3$	KaiA association constant $C_3$	0.003
$K_4$	KaiA dissociation constant $C_4$	0.01
$K_5$	KaiA dissociation constant $C_5$	0.03
$k_0$	KaiA-stimulated phosphorylation rate $C_0$	0.5/h
$k_1$	KaiA-stimulated phosphorylation rate $C_1$	0.5/h
$k_2$	KaiA-stimulated phosphorylation rate $C_2$	0.5/h
$k_3$	KaiA-stimulated phosphorylation rate $C_3$	0.5/h
$k_4$	KaiA-stimulated phosphorylation rate $C_4$	0.5/h
$k_5$	KaiA-stimulated phosphorylation rate $C_5$	0.5/h
$\tilde{b}_{2-4}$	Number KaiA dimers sequestered by $\tilde{C}_{1-4}$	2
$\tilde{b}_{0,5,6}$	Number KaiA dimers sequestered by $\tilde{C}_{0,5,6}$	0
$\tilde{K}_{1-4}$	KaiA dissociation constant $\tilde{C}_{1-4}$	0.000001
$\tilde{K}_{0,5,6}$	KaiA dissociation constant $\tilde{C}_{0,5,6}$	$\infty$
$c_T$	Total concentration of KaiC	1
$A_T$	Total concentration of KaiA	1

TABLE I: Parameter values of all the three computational models studied in the main text. The parameter values listed are those that maximize the mutual information  $I(p; t)$  between the phosphorylation level  $p$  and time  $t$ ; these values are nearly independent of the input-noise strength  $\sigma_s^2$ , and thus kept constant as  $\sigma_s^2$  is varied in the simulations corresponding to Fig. 2 of the main text. For these optimal parameters values, the intrinsic period of the uncoupled-hexamer model is  $T_0^{\text{opt}} \approx 23.1\text{h}$  while that of the coupled-hexamer model is  $T_0^{\text{opt}} \approx 25.1\text{h}$ . All three models are coupled to the input by multiplying the phosphorylation rates with  $s(t) = \sin(\omega) + \bar{s} + \eta_s(t)$ , where  $\bar{s} = 2$  and  $\eta_s(t)$  describes colored noise with strength  $\sigma_s^2$  and correlation time  $\tau_c$ ,  $\langle \eta_s(t)\eta_s(t') \rangle = \sigma_s^2 e^{-|t-t'|/\tau_c}$ . For Fig. 2 of the main text,  $\tau_c = 0.5\text{h}$ . Dissociation constants and protein concentrations are in units of the total KaiC concentration. Note that in the absence of oscillatory driving  $s(t) = \bar{s} = 2$ , meaning that in simulations of the non-driven systems the phosphorylation rates  $k_f$ ,  $k_i$ ,  $k_{ps}$ , still have to be multiplied by  $\bar{s} = 2$ .

**Optimal dephosphorylation rate** Specifically, the parameters  $k_f$  and  $k_b$  are set as follows: for a given input noise strength  $\sigma_s^2 = 1.0$ , we first fix the phosphorylation rate  $k_f$  and compute the mutual information  $I(p; t)$  between the phosphorylated fraction  $p(t) = x_p(t)/x_T$  and time  $t$  as a function of the dephosphorylation rate  $k_b$ ; we then repeat this procedure by varying  $k_f$ . The result is shown in Fig. 4B. Clearly, there exists an optimal value of  $k_b$  that maximizes  $I(p; t)$ . Moreover, the optimal value  $k_b^{\text{opt}}$  becomes independent of  $k_f$  when  $k_f$  becomes so small that the system enters the regime in which it responds linearly to changes in the mean input  $\bar{s}$ . We then fixed the phosphorylation rate to  $k_f = 0.01/\text{h}$ , and compute  $I(p; t)$  as a function of  $k_b$  for different levels of the input-noise strength, see Fig. 4C. It is seen that the optimal dephosphorylation rate  $k_b^{\text{opt}}$  is essentially independent of the input noise strength  $\sigma_s^2$ . In the simula-

tions corresponding to Fig. 2 of the main text, we therefore kept  $k_b$  constant at  $k_b^{\text{opt}} = 0.3/\text{h}$  and  $k_f$  constant at  $k_f = 0.01/\text{h}$  when we varied  $\sigma_s^2$ .

The observation that  $k_b^{\text{opt}}$  is independent of  $k_f$  and  $\sigma_s^2$  can be understood by noting that to maximize information transmission, the system should operate in the linear-response regime in which the mean output  $\bar{x}$  responds linearly to changes in the mean input  $\bar{s}$ . This regime tends to enhance information because it ensures that in the presence of a sinusoidal input, the output  $x_p(t)$  will not be distorted and be sinusoidal too. In this linear-response regime, the system can be analyzed analytically, see Eq. 43 in section below. This equation, which accurately predicts the optimum seen in Fig. 4B and Fig. 4C, reveals that the optimal dephosphorylation rate depends on the frequency of the driving signal,  $\omega$ , and the correlation time of the noise,  $\tau_c$ , but not on the

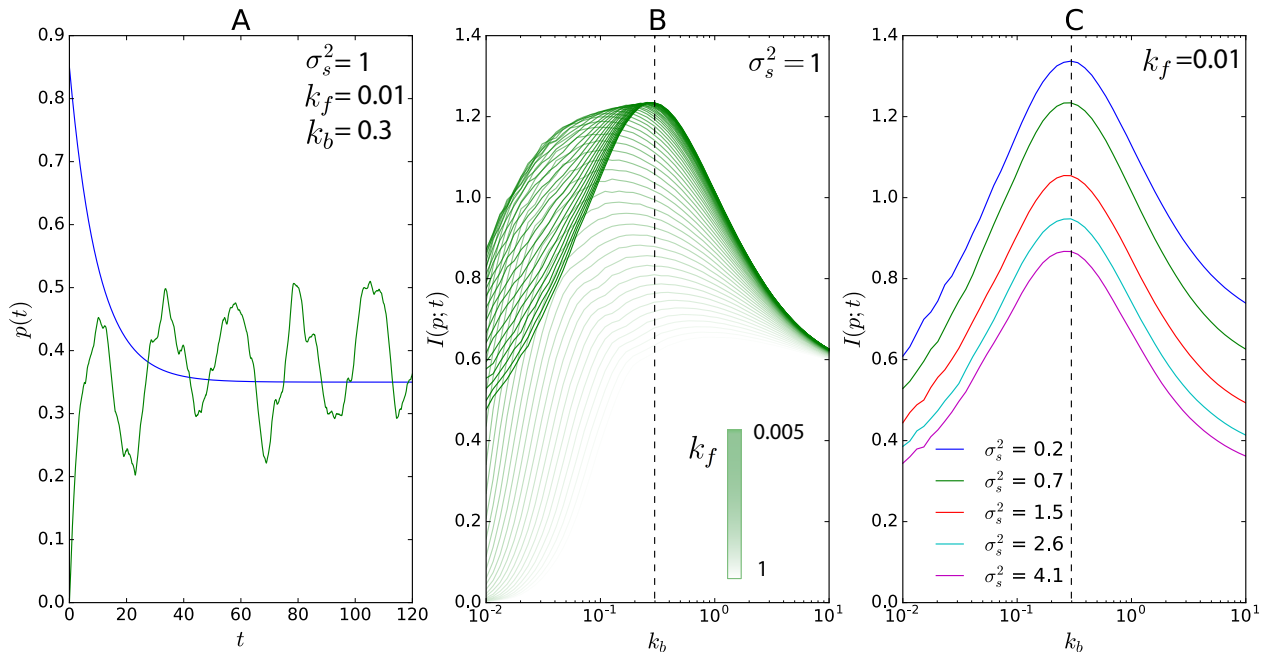


FIG. 4: The push-pull network. (A) Time trace of  $p(t)$  in the presence of driving (green line) and absence of driving (blue line). Please note that in the absence of driving, the system relaxes in an exponentially fashion to a stable fixed point. (B) The mutual information  $I(p;t)$  as a function of  $k_b$  for different values of  $k_f$  (see Eq. 7), for  $\sigma_s^2 = 1$ . It is seen that for each phosphorylation rate  $k_f$  there is an optimal dephosphorylation rate  $k_b$  that maximizes the mutual information  $I(p;t)$ . Moreover,  $I(p;t)$  increases as  $k_f$  decreases, but then saturates and hence becomes independent of  $k_f$  as the system enters the regime in which it responds linearly to the input  $s$ . The dashed line shows the optimal value of  $k_b^{\text{opt}} \approx 0.3/\text{h}$ , as predicted by Eq. 43. (C) The mutual information  $I(p;t)$  as a function of the dephosphorylation rate  $k_b$ , for different values of the input-noise strength  $\sigma_s^2$ , keeping the phosphorylation rate fixed at  $k_f = 0.01/\text{h}$ . The optimal dephosphorylation rate  $k_b^{\text{opt}} \approx 0.3/\text{h}$  (dashed line) is independent of  $\sigma_s^2$ , as predicted by Eq. 43. The input-noise correlation time  $\tau_c = 0.5\text{h}$ .

noise strength  $\sigma_s^2$  and the coupling  $\rho$  to the input signal, given by  $\rho = k_f x_T$ . Increasing the gain  $\rho$  amplifies not only the true signal, but also the noise in that signal (see also Eq. 5), such that the signal-to-noise ratio is unaltered. Indeed, increasing the gain only helps in the presence of internal noise, which here, however, is zero. Conversely, if intrinsic noise were present, simply decreasing  $k_f$  to bring the system in the optimal linear-response regime would lower the signal-to-noise ratio; however, the signal-to-noise ratio can always be enhanced by increasing  $x_T$ : this will not only increase the gain  $\rho = k_f x_T$  and thereby raise the output signal above the intrinsic noise, but also reduce the intrinsic noise itself.

We note that for (much) larger input-noise strength than that considered here, it might be beneficial to strongly increase the input signal and drive the system into the non-linear regime. This makes it possible to exploit the fact that the output  $p(t)$  is naturally bounded between zero and unity; the input noise can thus be tamed by continually pushing  $p(t)$  against either zero and unity. This generates, however, strongly non-sinusoidal, square-wave like oscillations, which are not experimentally observed [12]. We thus leave the regime of strong

driving for future work.

#### Uncoupled-hexamer model: Kai system of *Prochlorococcus*

**Background** The uncoupled-hexamer model (UHM) presented in the main text is a minimal model of the Kai system of the cyanobacterium *Prochlorococcus* and, possibly, the purple bacterium *Rhodospseudomonas palustris*. The well characterized clock of the cyanobacterium *S. elongatus* consists of three proteins, KaiA, KaiB and KaiC, which are all essential for sustaining free-running oscillations [3]. And, indeed, many cyanobacteria possess at least one copy of each *kai* gene. One exception is *Prochlorococcus*, which contains *kaiB* and *kaiC*, but misses a (functional) *kaiA* gene. Interestingly, in daily (12h:12h) light-dark (LD) cycles, the expression of many genes, including *kaiB* and *kaiC*, is rhythmic, but in constant conditions these rhythms damp very rapidly [5, 6]. Similar behavior is observed for the purple bacterium *R. palustris*, which possesses homologs of the *kaiB* and *kaiC* genes [2]: under LD conditions, the KaiC ho-



molog appears to be phosphorylated in a circadian fashion, but under constant conditions, the oscillations decay very rapidly; physiological activities, such as the nitrogen fixation rates, follow a similar pattern [2]. Of particular interest is the observation that under LD conditions but not under LL conditions, the growth rate is significantly reduced in the strain in which the *kaiC* homolog was knocked out [2]. This strongly suggests that the (homologous) Kai system plays a role as a timekeeping mechanism, which relies, however, on oscillatory driving.

**Model** Our model is inspired by the models that in recent years have been developed for *S. elongatus* [11, 12, 15–17]. These models share a number of characteristics that are essential for generating oscillations and entrainment (see also next section). The central clock component is KaiC, a hexamer, that can switch between an active state in which the phosphorylation level tends to rise and an inactive one in which it tends to fall. The model lacks KaiA because *Prochlororoccus* and *R. palustris* miss a functional *kaiA* gene [2, 5, 6]. In *S. elongatus*, KaiB does not directly affect the rates of phosphorylation and dephosphorylation, but mainly serves to stabilize the inactive state and mediate KaiA binding by inactive KaiC [16, 17]. KaiB is therefore not modelled explicitly [16, 17]. The main entrainment signal for *S. elongatus* is the ratio of ATP to ADP levels, which depends on the light intensity, and predominantly couples to KaiC in its active conformation [8, 9, 17, 18]. These observations give rise to the following chemical rate equations:

$$\dot{c}_0 = k_s \tilde{c}_0 - k_f s(t) c_0 \quad (8)$$

$$\dot{c}_i = k_f s(t) (c_{i-1} - c_i) \quad i \in (1, \dots, 5) \quad (9)$$

$$\dot{c}_6 = k_f s(t) c_5 - k_s c_6 \quad (10)$$

$$\dot{\tilde{c}}_6 = k_s c_6 - k_f \tilde{c}_6 \quad (11)$$

$$\dot{\tilde{c}}_i = k_b (\tilde{c}_{i+1} - \tilde{c}_i) \quad i \in (1, \dots, 5) \quad (12)$$

$$\dot{\tilde{c}}_0 = k_b \tilde{c}_1 - k_s \tilde{c}_0 \quad (13)$$

Here,  $c_i$ , with  $i = 0, \dots, 6$ , is the concentration of active  $i$ -fold phosphorylated KaiC in its active conformation, while  $\tilde{c}_i$  is the concentration of inactive  $i$ -fold phosphorylated KaiC. The quantity  $k_s$  is the conformational switching rate,  $k_b$  is the dephosphorylation rate of inactive KaiC, and  $k_f s(t)$  is the phosphorylation rate of active KaiC,  $k_f$ , times the input signal  $s(t)$ .

The output is the phosphorylation fraction of KaiC proteins (monomers), given by [11, 15, 17]

$$p(t) = \frac{1}{6} \frac{\sum_{i=0}^6 i(c_i + \tilde{c}_i)}{\sum_{i=0}^6 (c_i + \tilde{c}_i)}. \quad (14)$$

Fig. 5A shows a time trace of the phosphorylation level  $p(t)$  of both a driven and a non-driven uncoupled-hexamer model.

**Intrinsic frequency** Because the cycles of the different hexamers are not coupled via KaiA as in the coupled-hexamer model and in *S. elnogatus*, the system cannot sustain free-running oscillations. In this respect, the system is similar to the push-pull network in the sense that a perturbation of the non-driven system will relax to a stable fixed point. However, this model differs from the push-pull network in that it has a characteristic frequency  $\omega_0 = 2\pi/T_0$  with intrinsic period  $T_0$ , arising from the phosphorylation cycle of the KaiC hexamers. Consequently, while a perturbed (non-driven) push-pull network will relax exponentially to its stable fixed point, the uncoupled-hexamer model will, when not driven, relax in an oscillatory fashion to its stable fixed point with an intrinsic frequency  $\omega_0$  (see Fig. 5A). To predict the latter, we note that the dynamics of Eqs. 8-13 can be written in the form  $\dot{\mathbf{x}} = \mathbf{A}\mathbf{x}$ , and when all rate constants are equal,  $k_f \bar{s} = k_b = k_s$ , the eigenvalues and eigenvectors of  $\mathbf{A}$  can be computed analytically. The eigenvectors are complex exponentials. For a cycle with  $N$  sites with hopping rate  $k$ , the frequency associated with the lowest-lying eigenvalue is  $k \sin(2\pi/N)$ , which to leading order is  $2\pi k/N$ , corresponding to a period  $T_0 = N/k$ . Please note that this is also the period of a single multimer with  $N$  (cyclic) sites with  $N$  equal rates of hopping from one site to the next. We therefore expect that, to a good approximation, the intrinsic frequency  $\omega_0 = 2\pi/T_0$  of an ensemble of hexamers corresponds to the intrinsic period of a single hexamer:

$$T_0 \simeq \frac{2}{k_s} + \frac{6}{k_f \bar{s}} + \frac{6}{k_b} \simeq \frac{6}{k_f \bar{s}} + \frac{6}{k_b}, \quad (15)$$

where we recall that in the non-driven system the phosphorylation rate is  $k_f \bar{s}$ . We verified that this approximation is very accurate by fitting the relaxation of  $p(t)$  of the UHM to a function of the form  $e^{-\gamma t} \sin(\omega_0 t)$ , with  $\omega_0 = 2\pi/T_0$ . The intrinsic period  $T_0$  obtained in this way is to an excellent approximation given by Eq. 15.

#### Setting the parameters

The parameters were set as follows: the conformational switching rate  $k_s$  was set to be larger than the (de)phosphorylation rates  $k_s \gg \{k_f, k_b\}$ , as in the original models [11, 15, 17]. This leaves for a given input noise  $\eta_s$ , three parameters to be optimized: the phosphorylation rate  $k_f$ , the dephosphorylation rate  $k_b$ , and the mean input signal  $\bar{s}$ . The product  $k_f \bar{s}$  determines the mean phosphorylation rate, while  $k_f$  separately determines the strength of the forcing, i.e. the amplitude of the oscillations in the phosphorylation rate (see Eq. 5). The quantities  $k_f \bar{s}$  and  $k_b$  together determine the intrinsic frequency  $\omega_0 = 2\pi/T_0$  (see Eq. 15) and the symmetry of the phosphorylation cycle, set by the ratio  $r \equiv k_b/(k_f \bar{s})$ .

**Optimal intrinsic frequency** We therefore first computed for different input-noise strengths  $\sigma_s^2$ , the mutual information  $I(p; t)$  as a function of the ratio  $r = k_b/(k_f \bar{s})$  and a scaling factor  $q$  that scales both  $\bar{s}$  and  $k_b$ , keep-

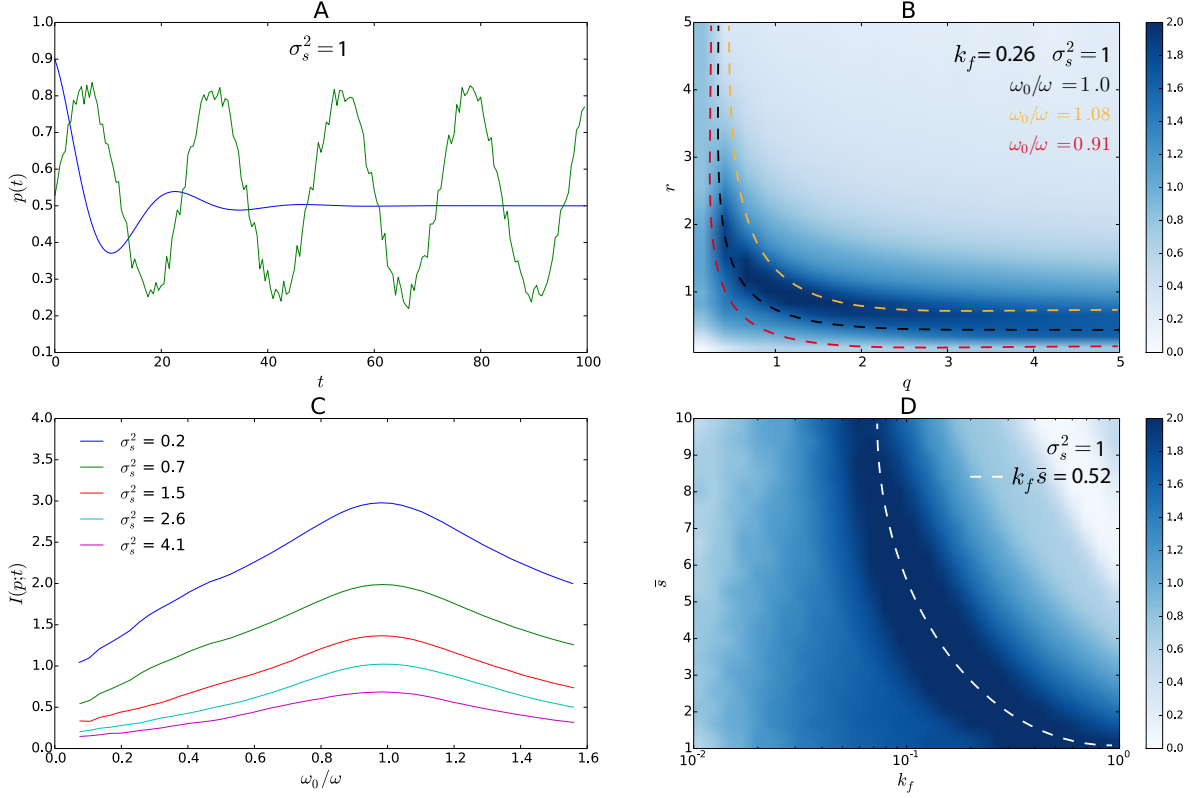


FIG. 5: The uncoupled-hexamer model. (A) Time trace of  $p(t)$  in the presence of driving (green line) and absence of driving (blue line). Please note that in the absence of driving, the system relaxes in an oscillatory fashion to a stable fixed point. (B) Heatmap of the mutual information  $I(p;t)$  as a function of the scaling factor  $q$  that scales both the dephosphorylation rate  $k_b$  and the mean phosphorylation rate  $k_f \bar{s}$  (see Eq. 5) and the ratio  $r = k_b/(k_f \bar{s})$  of these quantities. The mean phosphorylation rate  $k_f \bar{s}$  is changed by varying  $\bar{s}$  while keeping  $k_f$  constant; this ensures that the strength of the forcing, i.e. the amplitude of the phosphorylation-rate oscillations set by  $k_f$ , remains constant (see Eq. 5). Superimposed are contour lines of constant  $\omega_0 = \omega_0(q, r)$  (see Eq. 15). It is seen that in the regime where  $I(p;t)$  is high,  $I(p;t)$  is almost constant along these contour lines, showing that  $I(p;t)$  predominantly depends on  $\bar{s}$  and  $k_b$  via  $\omega_0$ . (C) The mutual information  $I(p;t)$  as a function of  $\omega_0$ , which was varied by scaling  $\bar{s}$  and  $k_b$  keeping  $r = k_b/(k_f \bar{s}) = 1$  and  $k_f = 0.26/\text{h}$ , for different values of the input-noise strength  $\sigma_s^2$ . It is seen that there exists an optimal intrinsic frequency  $\omega_0^{\text{opt}}$  that maximizes  $I(p;t)$ . Moreover,  $\omega_0^{\text{opt}}$  is nearly independent of  $\sigma_s^2$ , corresponding to an intrinsic period  $T_0 = 2\pi/\omega_0^{\text{opt}} \approx 23.1\text{h}$ . (D) The mutual information  $I(p;t)$  as a function of  $k_f$  and  $\bar{s}$ , keeping  $k_b = 0.52/\text{h}$  constant. Superimposed is the line along which  $k_f \bar{s} = 0.52/\text{h}$  and hence the intrinsic period  $T_0$  are constant (see Eq. 15). Along this line also  $I(p;t)$  is nearly constant, meaning that the strength of the forcing, set by  $k_f$ , is not very critical. This mirrors the behavior seen for the push-pull network (see Fig. 4). It is due to the fact that increasing the forcing raises not only the amplitude but also the noise, keeping the signal-to-noise ratio and hence the mutual information essentially unchanged. The noise correlation time  $\tau_c = 0.5\text{h}$ .

ing the strength of the forcing constant at  $k_f = 0.26/\text{h}$ . Fig. 5B shows the heatmap of  $I(p;t) = I(r, q)$  for  $\sigma_s^2 = 1$ , but qualitatively similar results were obtained for other values of  $\sigma_s^2$  (as discussed below). Since the intrinsic frequency  $\omega_0$  depends on both  $r$  and  $q$  (see Eq. 15), we have superimposed contourlines of constant  $\omega_0$ . Interestingly, the figure shows that in the relevant regime of high mutual information,  $I(p;t)$  follows the contourlines of constant  $\omega_0$ . This shows that  $I(p;t)$  depends on  $r$  and  $q$  predominantly through  $\omega_0(r, q)$ ,  $I(p;t) \approx I(\omega_0(r, q))$ . It demonstrates that the mutual information is primarily determined by the intrinsic period  $T_0$ —the time to com-

plete a single cycle—and not by the evenness of the pace around the cycle set by  $r$ .

To reveal the dependence of  $I(\omega_0)$  on  $\sigma_s^2$ , we show in panel C for different values of  $\sigma_s^2$ ,  $I(p;t)$  as a function of  $\omega_0$ , which was varied by scaling  $\bar{s}$  and  $k_b$  via the scaling factor  $q$ , keeping the ratio of  $k_f \bar{s}$  and  $k_b$  constant at  $r = 1$ . Clearly, there is an optimal frequency  $\omega_0^{\text{opt}} \approx 1.04\omega$  corresponding to an optimal  $k = k_f \bar{s} = k_b = 0.52/\text{h}$ , that maximizes the mutual information which is essentially independent of  $\sigma_s^2$ . In Fig. 2 of the main text, when we vary  $\sigma_s^2$ , we thus kept  $k = k_f \bar{s} = k_b = 0.52/\text{h}$  constant, with  $k_f = 0.26/\text{h}$  and  $\bar{s} = 2$ .

Interestingly, the optimal intrinsic frequency  $\omega_0^{\text{opt}}$  is not equal to the driving frequency  $\omega$ :  $\omega_0^{\text{opt}} > \omega$ , yielding an intrinsic period  $T_0^{\text{opt}} \approx 23.1\text{h}$  that is smaller than 24 hrs. This can be understood by analyzing the simplest model that mimics the uncoupled-hexamer model: the (damped) harmonic oscillator, which, like the uncoupled-hexamer model, is a linear system with a characteristic frequency. As described in , we expect generically for such a system that the optimal intrinsic frequency is larger than the driving frequency:  $\omega_0^{\text{opt}} > \omega$ . This is because while the amplitude  $A$  of the output (the “signal”) is maximal at resonance,  $\omega_0 = \omega$  (see Eq. 54), input-noise averaging is maximized (i.e. output noise  $\sigma_x$  minimized) for large  $\omega_0$  (see Eq. 59), such that the signal-to-noise ratio  $A/\sigma_x$  is maximal for  $\omega_0^{\text{opt}} > \omega$ .

**Mutual information is less sensitive to coupling strength** Lastly, while  $k_f\bar{s}$  and  $k_b$  are vital by setting the intrinsic period  $T_0$  (Eq. 15) that maximizes the mutual information (panels B and C of Fig. 5), we now address the importance of the coupling strength, which is set by  $k_f$  separately (see Eq. 5). To this end, we computed the mutual information  $I(p;t)$  as a function of  $k_f$  and  $\bar{s}$ , keeping the dephosphorylation rate constant at  $k_b = 0.52/\text{h}$ . Fig. 5D shows the result. It is seen that there is, as in panel B, a band along which the mutual information is highest. This band coincides with the superimposed dashed white line along which  $k_f\bar{s} = 0.52/\text{h}$  and hence  $T_0$  are constant (see Eq. 15). This shows that the mutual information  $I(p;t)$  is predominantly determined by the intrinsic period  $T_0$ : as the parameters are changed in a direction perpendicular to this line (and  $T_0$  changes most strongly), then  $I(p;t)$  falls dramatically. In contrast, along the dashed white line of constant  $T_0$ ,  $I(p;t)$  is nearly constant. It shows that the precise strength of the forcing, set by  $k_f$ , is not critical for the mutual information. This behavior mirrors that observed for the push-pull network. While increasing  $k_f$  increases the amplitude of the oscillations in  $p(t)$ , it also increases the noise, such that the signal-to-noise ratio and hence the mutual information are essentially unchanged. The same behavior is observed for the minimal model of this system, the harmonic oscillator, described in .

To sum up, in the simulations corresponding to Fig. 2 of the main text, we kept  $k_b = k_f\bar{s} = 0.52/\text{h}$ , with  $\bar{s} = 2$  and  $k_f = 0.26/\text{h}$ .

### Coupled-hexamer model: Kai system of *S. elongatus*

**Background** In contrast to the cyanobacterium *Prochlorococcus* and the purple bacterium *R. palustris*, the cyanobacterium *S. elongatus* harbors all three Kai proteins, KaiA, KaiB, and KaiC, and can (therefore) exhibit self-sustained, limit-cycle oscillations [3]. The circadian system combines a transcription-translation cycle (TTC) [23–25] with a protein phosphorylation cycle

(PPC) of KaiC [26], and in 2005 the latter was reconstituted in the test tube [4]. The dominant pacemaker appears to be the protein phosphorylation cycle [15, 27], although at higher growth rates the transcription-translation cycle is important for maintaining robust oscillations [15, 27]. Changes in light intensity induce a phase shift of the in-vivo clock and cause a change in the ratio of ATP to ADP levels [8]. Moreover, when these changes in ATP/ADP levels were experimentally simulated in the test tube, they induced a phase shift of the protein phosphorylation cycle which is similar to that of the wild-type clock [8]. These experiments indicate that the phosphorylation cycle is not only the dominant pacemaker, but also the cycle that couples the circadian system to the light input. We therefore focused on the protein phosphorylation cycle.

Due to the wealth of experimental data, the in-vitro protein phosphorylation cycle of *S. elongatus* has been modeled extensively in the past decade [11–17]. In [17] we presented a very detailed thermodynamically consistent statistical-mechanical model, which is based on earlier models [11, 15, 16] and can explain most of the experimental observations. The coupled-hexamer model (CHM) presented here is a minimal version of these models. It contains the necessary ingredients for describing the autonomous protein-phosphorylation oscillations and the coupling to the light input, i.e. the ATP/ADP ratio.

The model is similar to the uncoupled-hexamer model described in the previous section, with KaiC switching between an active state in which the phosphorylation level tends to rise and an inactive in which it tends to fall. The key difference between the two systems is that the CHM also harbors KaiA, which synchronizes the oscillations of the individual hexamers via the mechanism of differential affinity [11, 12], allowing for self-sustained oscillations. Specifically, KaiA is needed to stimulate phosphorylation of active KaiC, yet inactive KaiC can bind KaiA too. Consequently, inactive hexamers that are in the dephosphorylation phase of the phosphorylation cycle—the laggards—can take away KaiA from those KaiC hexamers that have already finished their phosphorylation cycle—the front runners. These front runners are ready for a next round of phosphorylation, but need to bind KaiA for this. By strongly binding and sequestering KaiA, the laggards can thus take away KaiA from the front runners, thereby forcing them to slow down. This narrows the distribution of phosphoforms, and effectively synchronizes the phosphorylation cycles of the individual hexamers [11]. The mechanism appears to be active not only during the inactive phase, but also during the active phase: KaiA has a higher binding affinity for less phosphorylated KaiC [11, 16]. Since KaiB serves to mainly stabilize the inactive state and mediate the sequestration of KaiA by inactive KaiC, KaiB is, as in the UHM and following [16, 17], only modelled implicitly.

**Model** Since computing the mutual information accu-

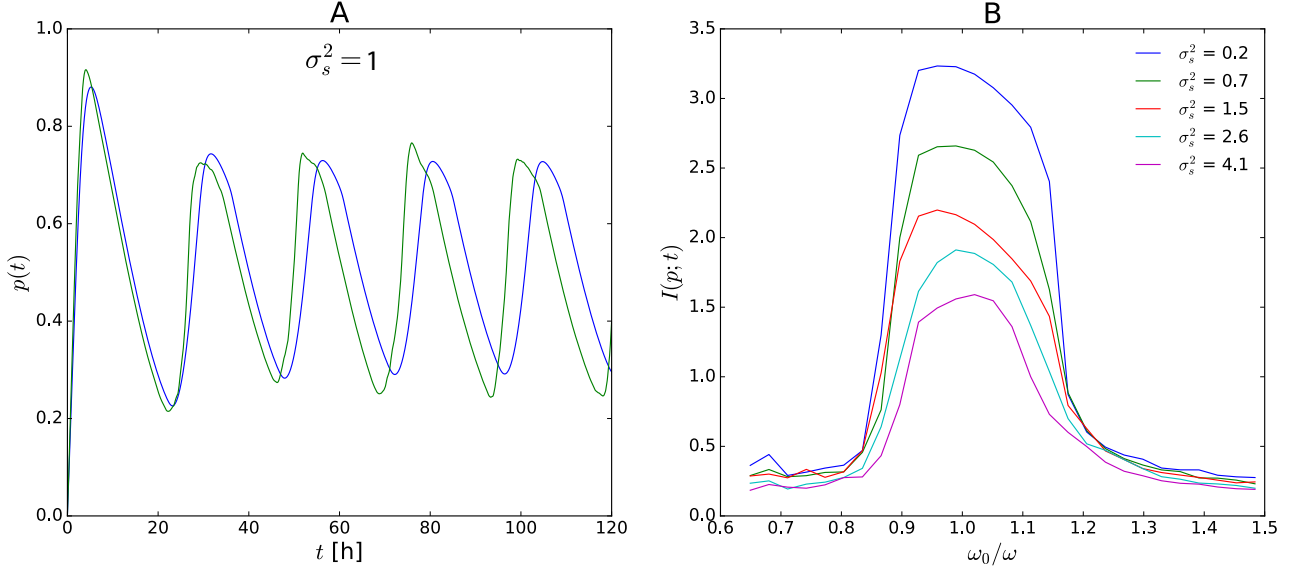


FIG. 6: The coupled-hexamer model. (A) Time trace of  $p(t)$  in the presence of driving (green line) and absence of driving (blue line). In the absence of driving, the system exhibits stable, limit-cycle oscillations. (B) The mutual information  $I(p; t)$  as a function of the intrinsic frequency, which was varied by scaling all phosphorylation rates  $\{k_{ps}, k_i, k_b\}$  by a factor  $q$ . It is seen that there exists an optimal (de)phosphorylation rate that maximizes  $I(p; t)$ , which weakly depends on  $\sigma_s^2$ . It corresponds to an intrinsic period  $T_0 = 25.1$ h of the free-running clock. The noise correlation time  $\tau_c = 0.5$ h.

rately requires very long simulations, we sought to develop a minimal version of the PPC model presented in [11, 15, 28], which can describe a wealth of data including the concentration dependence of the self-sustained oscillations and the coupling to ATP/ADP [11, 18, 28]. This model is described by the following chemical rate equations:

$$\dot{c}_0 = k_s \tilde{c}_0 - s(t)c_0 \left[ k_0 \frac{A}{A + K_0} + k_{ps} \frac{K_0}{A + K_0} \right] \quad (16)$$

$$\begin{aligned} \dot{c}_i = s(t)c_{i-1} \left[ k_{i-1} \frac{A}{A + K_{i-1}} + k_{ps} \frac{K_{i-1}}{A + K_{i-1}} \right] \\ - s(t)c_i \left[ k_i \frac{A}{A + K_i} + k_{ps} \frac{K_i}{A + K_i} \right] \quad i \in (1, \dots, 5) \end{aligned} \quad (17)$$

$$\dot{c}_6 = s(t)c_5 \left[ k_5 \frac{A}{A + K_5} + k_{ps} \frac{K_5}{A + K_5} \right] - k_s c_6 \quad (18)$$

$$\dot{\tilde{c}}_6 = k_s c_6 - k_b \tilde{c}_6 \quad (19)$$

$$\dot{\tilde{c}}_i = k_b (\tilde{c}_{i+1} - \tilde{c}_i) \quad i \in (1, \dots, 5) \quad (20)$$

$$\dot{\tilde{c}}_0 = k_b \tilde{c}_1 - k_s \tilde{c}_0 \quad (21)$$

$$A = A_T - \sum_{j=0}^5 c_j \frac{A}{A + K_j} - \sum_{j=0}^6 b_j \tilde{c}_j \frac{A^{b_j}}{A^{b_j} + \tilde{K}_j} \quad (22)$$

Here,  $c_i$  and  $\tilde{c}_i$  are the concentrations of active and inactive  $i$ -fold phosphorylated KaiC,  $A$  is the concentration of free KaiA. The rates  $k_i$  are the rates of KaiA-stimulated phosphorylation of active KaiC and  $k_{ps}$  is the spontaneous phosphorylation rate of active KaiC when KaiA is

not bound. Please note that both rates are multiplied by the input signal  $s(t)$ , since both rates depend on the ATP/ADP ratio [17]. The dephosphorylation rate  $k_b$  is independent of the ATP/ADP ratio [16, 17] and hence  $k_b$  is not multiplied with  $s(t)$ . As in the UHM,  $k_s$  is the conformational switching rate. The last equation, Eq. 22, gives the concentration  $A$  of free KaiA under the quasi-equilibrium assumption of rapid KaiA (un)binding by active KaiC with affinity  $K_i$  (second term right-hand side) and rapid binding of KaiA by inactive KaiC, where each  $i$ -fold phosphorylated inactive KaiC hexamer can bind  $b_i$  KaiA dimers (last term right-hand side Eq. 22). The mechanism of differential affinity is implemented via two ingredients: 1) the dissociation constant of KaiA binding to active KaiC,  $K_i$ , depends on the phosphorylation level  $i$ , with less phosphorylated KaiC having a higher binding affinity:  $K_i < K_{i+1}$  [11, 16, 17]; 2) inactive KaiC can strongly bind and sequester KaiA [11, 16, 17]; this is modeled by the last term in Eq. 22.

**Autonomous oscillations** Fig. 6A shows a time trace of  $p(t)$  (Eq. 14) for both a driven and a non-driven coupled-hexamer model. Clearly, in contrast to the push-pull network and the uncoupled-hexamer model, this system exhibits free running simulations. Note also that the autonomous oscillations are slightly asymmetric as observed experimentally, and as shown also by the detailed models on which this minimal model is based [11, 15]. Lastly, while the driving signal is sinusoidal, the output signal of the driven system remains non-sinusoidal. This is because this system is non-linear; this behavior

is indeed in marked contrast to the behavior seen for the linear UHM (see Fig. 5) and that of the PPN (Fig. 4) which operates in the linear regime. The slight asymmetry in the oscillations also explains why in the regime of very low noise, this system has a slightly lower mutual information than that of push-pull network or the uncoupled-hexamer model, as seen in Fig. 1 of the main text.

### Setting the parameters

We first set the parameters to get autonomous oscillations, keeping  $s(t) = \bar{s} = 2$ . These parameters were inspired by the parameters of the model upon which the current model is built [11]. Specifically, the KaiA binding affinity of active KaiC, given by  $K_i$ , was chosen such that it obeys differential affinity,  $K_0 < K_1 < K_2 < K_3 < K_4 < K_5$ , as in the PPC model of [11, 15, 28]. In addition, in our model,  $b_i = 2$  for  $i = 1, 2, 3, 4$  and  $b_i = 0$  for  $i = 0, 5, 6$ , meaning that  $i = 1 - 4$  fold phosphorylated inactive KaiC hexamers can each bind two KaiA dimers with strong affinity  $\tilde{K}_i = \tilde{K}$ . The conformational switching rate  $k_s$  was set to be higher than all the (de)phosphorylation rates,  $k_s \gg \{k_i, k_{ps}, k_b\}$  and the values of  $k_i, k_{ps}, k_b$  were, again apart from a scaling factor to set the optimal intrinsic frequency, identical to those of the PPC model of [11, 16, 28]. These parameter values allowed for robust free-running oscillations (see Fig. 6A) in near quantitative agreement with the oscillations of the more detailed PPC model of [11, 16, 28].

**Optimal intrinsic frequency** We then studied the driven system. We varied the intrinsic frequency  $\omega_0$  of the autonomous oscillations by varying all (de) phosphorylation rates  $\{k_i, k_{ps}, k_b\}$  by a constant factor and computed the mutual information  $I(p; t)$  as a function of this factor and hence  $\omega_0$ . The result is shown in Fig. 6B. Clearly, as for the uncoupled-hexamer model, there exists an optimal intrinsic frequency  $\omega_0^{\text{opt}}$  that maximizes the mutual information  $I(p; t)$ . The optimal intrinsic frequency depends on the input-noise strength: for low input noise,  $\omega_0^{\text{opt}} < \omega$ , but then  $\omega_0^{\text{opt}}$  increases with  $\sigma_s^2$  to become similar to  $\omega$  in the high noise regime. We also see, however, that the dependence of  $\omega_0^{\text{opt}}$  on  $\sigma_s^2$  is weak (Fig. 6B), and we therefore kept the parameters in the simulations corresponding to Fig. 2 of the main text, constant. Lastly, we note that we have verified that, as observed for the uncoupled-hexamer model, the key parameter for optimizing  $I(p; t)$  is  $k_f \bar{s}$ , because that sets the intrinsic frequency, and not  $k_f$  and  $\bar{s}$  separately. Table I gives an overview of all the parameters; this parameter set thus corresponds to a free-running rhythm of  $\omega_0^{\text{opt}} = 0.96\omega$ , corresponding to an intrinsic period  $T_0 = 25.1\text{h}$ .

### Robustness of observations

We have tested the robustness of our principal result, shown in Fig. 2 of the main text, by varying a number

of key parameters. We first varied the correlation time  $\tau_c$  of the noise, see Fig. 7A. Clearly, the main result is robust to variations in the value of  $\tau_c$ : in the limit of small input-noise  $\sigma_s^2$  all three time-keeping systems are equally accurate, while for large input noise the bonafide clock is far superior. We have also varied the nature of the input signal. Specifically, instead of a sinusoidal signal we have also studied a truncated sinusoidal signal  $s(t)$ , which drops to zero for 12 hours during the night but is a half-sinusoid for 12 hours during the day:

$$s(t) = h(t) \{\sin(\omega t) + \eta_s(t)\}, \quad (23)$$

where  $h(t) = 0$  for  $0 < t < 12$  and  $h(t) = 1$  for  $12 < t < 24$ . The result is shown in Fig. 7B. It is seen that the principal result of Fig. 2 of the main text is also insensitive to the precise choice of the input signal.

The robustness of our principal observations indicate they are universal and should be observable in minimal generic models. These are described in the next sections.

## Computing the mutual information

The mutual information is computed using the following relation

$$I(p; t) = H(p) - \langle H(p|t) \rangle_t, \quad (24)$$

where

$$H(p) = - \int_0^1 dp P(p) \log P(p) \quad (25)$$

is the entropy of the distribution  $P(p)$  of the phosphorylation fraction  $p(t)$  and

$$\langle H(p|t) \rangle_t = - \frac{1}{T} \int_0^T dt \int_0^1 dp P(p|t) \log P(p|t) \quad (26)$$

is the average of the conditional entropy of  $P(p|t)$ , with  $P(p|t)$  the conditional distribution of  $p$  given  $t$ . In numerically computing the mutual information, we have verified that the results are independent of the bin size of the distribution of  $p$ , following the approach of [32]. We also note that when the input noise is exactly zero, the mutual information diverges because the system is deterministic. The highest mutual information reported corresponds to the smallest input-noise level modeled, which is non-zero, leading to a finite mutual information.

## ANALYTICAL MODELS

### Push-pull network

The equation for the push-pull network is

$$\dot{x}_p = k_f s(t)(x_T - x_p(t)) - k_b x_p \quad (27)$$

$$\simeq k_f s(t)x_T - k_b x_p, \quad (28)$$

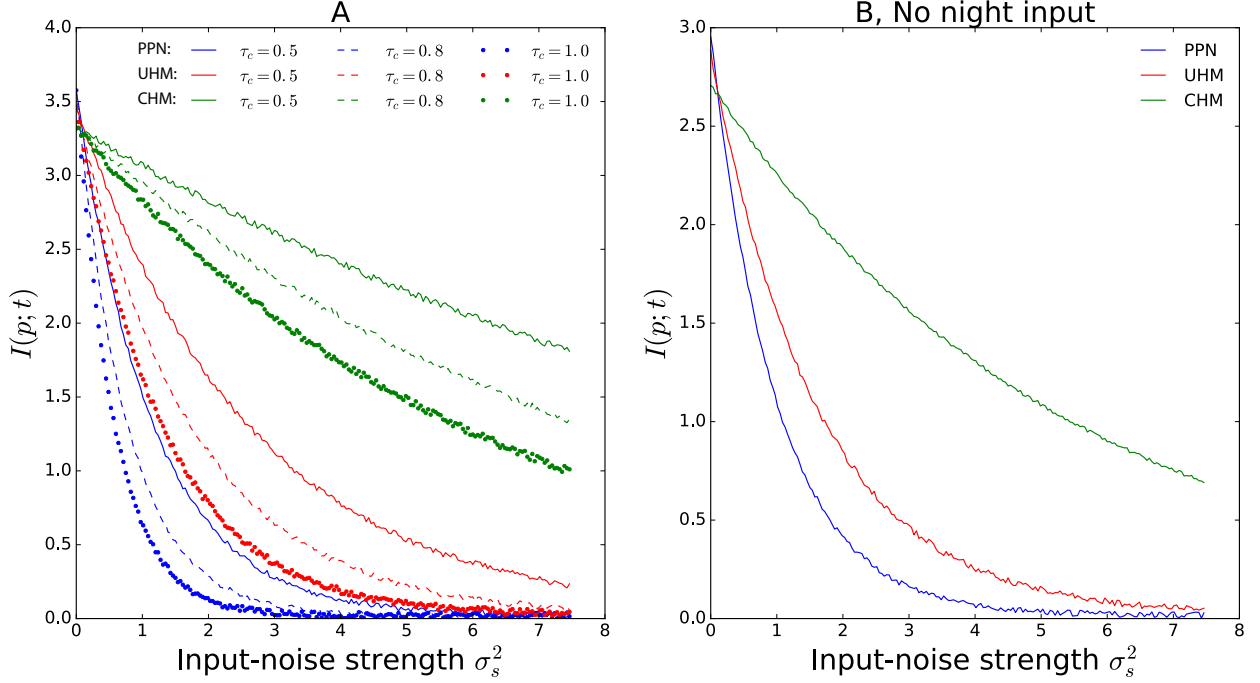


FIG. 7: Robustness of the principal result of our paper, Fig. 2 of the main text. (A) Robustness to correlation time of the input noise. It is seen that increasing the correlation time  $\tau_c$  of the input noise lowers the mutual information  $I(p; t)$ . This is because a higher correlation time impedes noise averaging [29–31]. Yet, for all values of  $\tau_c$  the result of Fig. 2 of the main text is recapitulated: when the input-noise strength  $\sigma_s^2$  is low, all readout systems are equally accurate; yet, in the high noise regime, the coupled-hexamer model is superior. (B) Robustness to the shape of the input signal. Here, the input is a truncated sinusoidal signal so that during the night  $s(t) = 0$ , while during the day  $s(t)$  is a half sinusoid (see Eq. 23). As expected, shutting off the driving during the night lowers the mutual information (compare with panel A). More strikingly, in the regime of low input noise, all readout systems are again equally informative on time. Clearly, the push-pull network and uncoupled-hexamer model do not need to be driven constantly; it is sufficient that the light drives the phosphorylation of the readout proteins during the day, so that they can dephosphorylate spontaneously during the night. In the regime of high input-noise, the coupled-hexamer system is again optimal. In panel B, the noise correlation time  $\tau_c = 0.5$ h. Other parameters are in Table I.

where in the last equation we have assumed that  $x_T \gg x_p$ , which is the case when  $k_f s(t) \ll k_b$ . In this regime, the push-pull network operates in the linear regime, leading to sinusoidal oscillations, which tend to enhance information transmission [19]. In what follows, we write, to facilitate comparison with other studies on noise transmission [19, 33]  $\rho \equiv k_f x_T$ ,  $\mu = k_b$  and, for notational convenience,  $x_p = x$ . We thus study

$$\dot{x} = \rho s(t) - \mu x(t). \quad (29)$$

The equation can be solved analytically to yield

$$x(t) = \int_{-\infty}^t dt' \chi(t-t') s(t'), \quad (30)$$

with  $\chi(t-t') = \rho e^{-\mu(t-t')}$ . With the input signal given by

$$s(t) = \sin(\omega t) + \bar{s} + \eta_s(t), \quad (31)$$

the output is

$$x(t) = A \sin(\omega t - \phi) + \bar{x} + \eta_x(t) \quad (32)$$

where the amplitude is

$$A = \frac{\rho}{\sqrt{\mu^2 + \omega^2}}, \quad (33)$$

the phase difference of the output with the input is

$$\phi = \arctan(\omega/\mu), \quad (34)$$

the mean is

$$\bar{x} = \rho \bar{s} / \mu \quad (35)$$

and the noise is

$$\eta_x = \rho \int_{-\infty}^t dt' e^{-\mu(t-t')} \eta_s(t'). \quad (36)$$

The variance of the output, assuming the system is in steady state, is then

$$\sigma_x^2 = \langle (x(0) - \bar{x}(0))^2 \rangle \quad (37)$$

$$= \rho^2 \int_{-\infty}^0 \int_{-\infty}^0 dt dt' e^{\mu(t+t')} \langle \eta_s(t) \eta_s(t') \rangle. \quad (38)$$

Assuming that the input noise has variance  $\sigma_s^2$  and decays exponentially with correlation time  $\tau_c = \lambda^{-1}$ , meaning that  $\langle \eta_s(t) \eta_s(t') \rangle = \sigma_s^2 e^{-\lambda|t-t'|}$ , the variance of the output is

$$\sigma_x^2 = \rho^2 \sigma_s^2 \left[ \int_{-\infty}^0 \int_{-\infty}^t dt dt' e^{\mu(t+t')} e^{-\lambda(t-t')} + \right. \quad (39)$$

$$\left. \int_{-\infty}^0 \int_t^0 dt dt' e^{\mu(t+t')} e^{-\lambda(t-t')} \right] \quad (40)$$

$$= g^2 \frac{\mu}{\mu + \lambda} \sigma_s^2, \quad (41)$$

with the gain given by  $g \equiv \rho/\mu$ .

The signal-to-noise ratio  $A/\sigma_x$  is then

$$\frac{A}{\sigma_x} = \sqrt{\frac{\mu(\mu + \lambda)}{\mu^2 + \omega^2}} \frac{1}{\sigma_s}, \quad (42)$$

which has a maximum at the optimal relaxation rate [19]

$$\mu^{\text{opt}} = \frac{\omega^2}{\lambda} \left( 1 + \sqrt{1 + (\lambda/\omega)^2} \right). \quad (43)$$

This optimum arises from a trade-off between the amplitude, which increases as  $\mu$  increases, and input-noise averaging, which improves as  $\mu$  decreases. Another point to note is that the optimal signal-to-noise ratio does not depend on  $\rho = k_f x_T$ , and hence not on  $k_f$  and  $x_T$ : while increasing  $\rho$  increases the amplitude of the signal, it also amplifies the noise in the input signal. Increasing the gain  $\rho$  (via  $x_T$  and/or  $k_f$ ) only helps in the presence of intrinsic noise, because increasing the amplitude of the signal helps to raise the signal above the intrinsic noise [19]. However, in the deterministic models considered in this study, the intrinsic noise is zero.

### The harmonic oscillator and the uncoupled-hexamer model

The uncoupled-hexamer model (UHM) is linear. Moreover, because each hexamer has a phosphorylation cycle with a characteristic oscillatory frequency  $\omega_0$ , this system is akin to the harmonic oscillator. Indeed, when not driven, both the UHM and the harmonic oscillator relax in an oscillatory fashion to a stable fixed point. To develop intuition on the behavior of the UHM, we therefore here analyze the behavior of a harmonic oscillator driven by a noisy sinusoidal signal.

The equation of motion of the driven harmonic oscillator is

$$\ddot{x} + \omega_0^2 x + \gamma \dot{x} = \rho s(t), \quad (44)$$

where  $\omega_0$  is the characteristic frequency,  $\gamma$  is the friction and  $\rho$  describes the strength of the coupling to the input signal  $s(t)$ . We assume that  $s(t) = \sin(\omega t) + \eta_s(t)$ . We note that while the undriven harmonic oscillator is isomorphic to the undriven UHM, their coupling to the input is different: in the UHM, the hexamers are, motivated by the Kai system [8, 9], only coupled to the input during their active phosphorylation phase, while the harmonic oscillator is coupled continuously; moreover, in the harmonic oscillator the noise is additive, while in the UHM the signal multiplies the phosphorylation rate, leading to multiplicative noise. Yet, the behavior of the two models is qualitatively similar, as discussed below.

Solving Eq. 44 in Fourier space yields  $\tilde{x}(\omega) = \tilde{\chi}(\omega) \tilde{s}(\omega)$ , with

$$\tilde{\chi}(\omega) = \frac{\rho}{\omega_0^2 - \omega^2 - i\omega\gamma}. \quad (45)$$

Hence, the time evolution of  $x(t)$  is

$$x(t) = \frac{1}{2\pi} \int_{-\infty}^{\infty} d\omega e^{-i\omega t} \tilde{\chi}(\omega) s(\omega) \quad (46)$$

$$= \frac{\rho}{2\pi} \int_{-\infty}^{\infty} d\omega \int_{-\infty}^{\infty} dt' \frac{e^{i\omega(t'-t)} s(t')}{\omega_0^2 - \omega^2 - i\omega\gamma}. \quad (47)$$

We do the integral over  $\omega$  first. The integrand has poles at

$$\omega = \frac{-i\gamma}{2} \pm \sqrt{\omega_0^2 - \frac{\gamma^2}{4}} \equiv \frac{-i\gamma}{2} \pm \omega_1. \quad (48)$$

This yields

$$x(t) = \frac{\rho}{2\pi} \int_{-\infty}^{\infty} s(t') \theta(t-t') (2\pi i) \times \quad (49)$$

$$\left[ \frac{e^{i(-i\frac{\gamma}{2} + \omega_1)(t'-t)}}{2\omega_1} - \frac{e^{i(-i\frac{\gamma}{2} - \omega_1)(t'-t)}}{2\omega_1} \right] \quad (50)$$

$$= \frac{\rho}{\omega_1} \int_{-\infty}^t dt' e^{-\frac{\gamma}{2}(t-t')} \sin(\omega_1(t-t')) s(t'). \quad (51)$$

With  $s(t) = \sin(\omega t)$ , this yields

$$x(t) = \frac{-\gamma\omega \cos[\omega t] + (-\omega^2 + \omega_0^2) \sin[\omega t]}{\gamma^2\omega^2 + (\omega^2 - \omega_0^2)^2} \quad (52)$$

This can also be rewritten as

$$x(t) = A \sin(\omega t + \phi), \quad (53)$$

with the amplitude given by

$$A = \frac{\rho}{\sqrt{\gamma^2\omega^2 + (\omega^2 - \omega_0^2)^2}} \quad (54)$$

and the phase given by

$$\phi = \arctan \left[ \frac{-4\gamma\omega}{\gamma^2 + 4(\omega_1^2 - \omega^2)} \right]. \quad (55)$$

Eq. 54 shows that the amplitude increases as the friction decreases and that the amplitude is maximal when the intrinsic frequency equals the driving frequency; in fact, when  $\gamma \rightarrow 0$  and  $\omega_0 = \omega$ , the amplitude diverges.

With an input noise with variance  $\sigma_s^2$  and decay rate  $\lambda$ , the noise in the output,  $\sigma_x^2 = \langle \delta x^2(0) \rangle$ , is given by

$$\sigma_x^2 = \frac{\rho^2}{\omega_1^2} \int_{-\infty}^0 dt \int_{-\infty}^0 dt' e^{\frac{\gamma}{2}(t+t')} \sin(\omega_1 t) \sin(\omega_1 t') \langle \eta_s(t) \eta_s(t') \rangle \quad (56)$$

$$= \frac{\rho^2 \sigma_s^2}{\omega_1^2} \left[ \int_{-\infty}^0 dt \int_{-\infty}^t dt' e^{\frac{\gamma}{2}(t+t')} \sin(\omega_1 t) \sin(\omega_1 t') e^{-\lambda(t-t')} + \int_{-\infty}^0 dt \int_t^0 dt' e^{\frac{\gamma}{2}(t+t')} \sin(\omega_1 t) \sin(\omega_1 t') e^{-\lambda(t'-t)} \right] \quad (57)$$

$$= \rho^2 \sigma_s^2 \frac{16(\gamma + \lambda)}{\gamma[(\gamma + 2\lambda)^2 + 4\omega_1^2](\gamma^2 + 4\omega_1^2)} \quad (58)$$

$$= \rho^2 \sigma_s^2 \frac{(\gamma + \lambda)}{\gamma \omega_0^2 [\lambda(\gamma + \lambda) + \omega_0^2]} \quad (59)$$

This expression shows that the noise diverges for all frequencies when the friction  $\gamma \rightarrow 0$ . It also shows that the noise diverges for  $\omega_0 \rightarrow 0$  for all values of  $\gamma$ , or, conversely, that it goes to zero for  $\omega_0 \rightarrow \infty$ . This can be understood by imagining a particle with mass  $m = 1$  in a harmonic potential well with spring constant  $k$ , giving a resonance frequency  $\omega_0^2 = k/m = k$ , which is buffeted by stochastic forces: its variance decreases as the spring constant  $k$  and intrinsic frequency  $\omega_0$  increase.

Figs. 8 and 9 show the amplitude  $A$ , noise  $\sigma_x^2$ , and signal-to-noise ratio  $A/\sigma_x$  for the harmonic oscillator. Clearly, the amplitude is maximal at resonance, diverging when  $\gamma \rightarrow 0$  (Fig. 8A). The noise is maximal at  $\omega_0 \rightarrow 0$ , and also diverges for all frequencies when  $\gamma \rightarrow 0$  (Fig. 8B). However, the amplitude rises more rapidly as  $\gamma \rightarrow 0$  than the noise does, leading to a global optimum of the signal-to-noise ratio for  $\omega_0 = \omega$  and  $\gamma \rightarrow 0$  (Fig. 8C). However, biochemical networks have, in general, a finite friction, and then the optimal intrinsic frequency is off resonance, as most clearly seen in Fig. 9. In fact, since the noise is minimized for  $\omega_0 \rightarrow \infty$  while the amplitude is maximized at resonance,  $\omega_0 = \omega$ , the optimal frequency  $\omega_0^{\text{opt}}$  that maximizes the signal-to-noise ratio is in general  $\omega_0^{\text{opt}} > \omega$ , as indeed also observed for the uncoupled hexamer model (see Fig. 5B).

Because noise is commonly modeled as Gaussian white noise, as in our Stuart-Landau model below, rather than colored noise as assumed here, we also give, for completeness, the expression for  $\sigma_x^2$  when the input noise is

Gaussian and white,  $\langle \eta_s(t) \eta_s(t') \rangle = \sigma_{s,\text{white}}^2 \delta(t - t')$ . It is

$$\sigma_x^2 = \frac{\rho^2 \sigma_{s,\text{white}}^2}{2\gamma \omega_0^2}. \quad (60)$$

This is consistent with Eq. 59, by noting that the integrated noise strength of the colored noise is  $2 \int_0^\infty dt \sigma_s^2 e^{-\lambda t} = 2\sigma_s^2/\lambda$ , while the integrated noise strength of the white noise case is  $\sigma_{s,\text{white}}^2$ . Indeed, with this identification, Eq. 59 in the limit of large  $\lambda$  reduces to the above expression for the white noise case.

### Comparison between push-pull network and harmonic oscillator in the high friction limit

Intuitively, one would expect that in the high-friction limit the harmonic oscillator performs similarly to the push-pull network. The signal-to-noise ratio  $\text{SNR} = A/\sigma_x$  indeed becomes the same in this limit. However, the amplitude and the noise separately scale differently, because the friction in the harmonic oscillator also reduces the strength of the signal and the noise: in the high-friction limit, the equation of motion of the harmonic oscillator becomes  $\dot{x}_{\text{HO}} = \rho s(t)/\gamma - \omega_0^2/\gamma x(t) + \rho \eta_s(t)/\gamma$ , showing that the friction renormalizes both the signal and the noise. However, such a renormalization of both the signal and the noise should not affect the signal-to-noise ratio. Moreover, we now see that in this high-friction limit the harmonic oscillator relaxes with a rate  $\omega_0^2/\gamma$ , which is to be compared with  $\mu$  of the push-pull network, for which  $\dot{x}_{\text{PP}} = \rho s(t) - \mu x(t) + \rho \eta_s(t)$ . From this we can anticipate that while the amplitude and the noise will be different, the signal-to-noise ratio will be the same. Concretely, in the high-friction limit the amplitude, the noise and the signal-to-noise ratio of the harmonic oscillator become

$$A^{\text{HO}} = \frac{\rho}{\gamma \omega} \quad (61)$$

$$\sigma_x^{\text{HO}} = \frac{\rho \sigma_s}{\omega_0 \sqrt{\gamma \lambda}} \quad (62)$$

$$\text{SNR}^{\text{HO}} = \sqrt{\frac{\omega_0^2}{\gamma} \frac{\sqrt{\lambda}}{\omega}} = \frac{\sqrt{\mu \lambda}}{\omega}, \quad (63)$$

where in the last line we have made the identification  $\mu = \omega_0^2/\gamma$ . For the push-pull network, the corresponding quantities, in the limit that  $\mu \rightarrow 0$ , are

$$A^{\text{PP}} = \frac{\rho}{\mu} \quad (64)$$

$$\sigma_x^{\text{PP}} = \frac{\rho \sigma_s}{\mu \lambda} \quad (65)$$

$$\text{SNR}^{\text{PP}} = \frac{\sqrt{\mu \lambda}}{\omega}. \quad (66)$$

Clearly, the signal-to-noise ratio of the two models are the same in the limit of high friction.



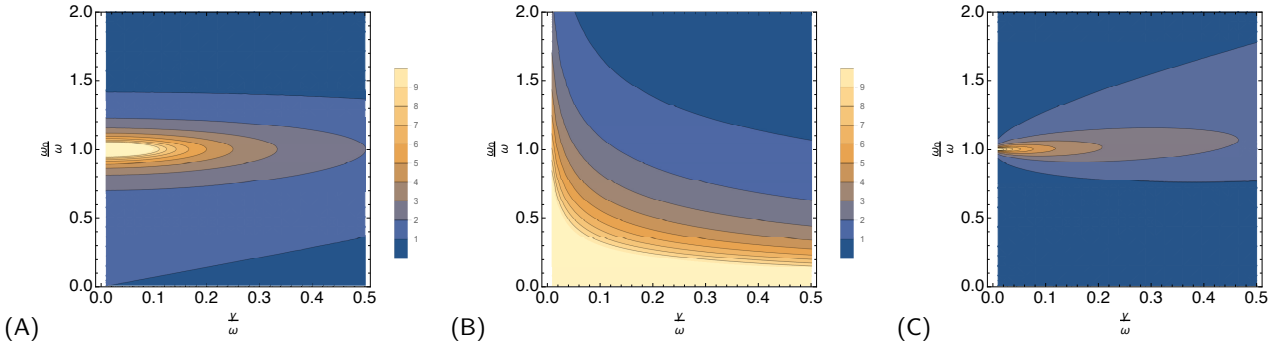


FIG. 8: The amplitude (A), standard deviation  $\sigma_x$  (B), and signal-to-noise ratio  $A/\sigma_x$  (C) as a function of the the intrinsic frequency  $\omega_0$  and friction  $\gamma$  for the harmonic oscillator. It is seen that the amplitude peaks when  $\gamma = 0$  and the intrinsic frequency equals the driving frequency,  $\omega_0 = \omega$  (A). The noise peaks at  $\gamma = 0$  and at  $\omega_0 = 0$  (B). Because the amplitude peaks at  $\omega_0 = \omega$ , while the noise peaks at  $\omega_0 = 0$ , there is an optimal intrinsic frequency  $\omega_0^{\text{opt}} > \omega$  that maximizes the signal-to-noise ratio (C). See also Fig. 9.

Fig. 10 compares the behavior of the harmonic oscillator against that of the push-pull system. Clearly, for small  $\gamma$ , the signal-to-noise ratio SNR of the harmonic oscillator is larger than that of the push-pull network, showing that building an oscillatory tendency with a resonance frequency into a readout system can enhance the signal-to-noise ratio. However, in the large-friction limit, the SNR is the same of both models, as expected.

### Weakly non-linear oscillator and the coupled-hexamer model

The coupled-hexamer model (CHM) is a non-linear oscillator that can sustain autonomous limit-cycle oscillations in the absence of any driving. Here, we describe

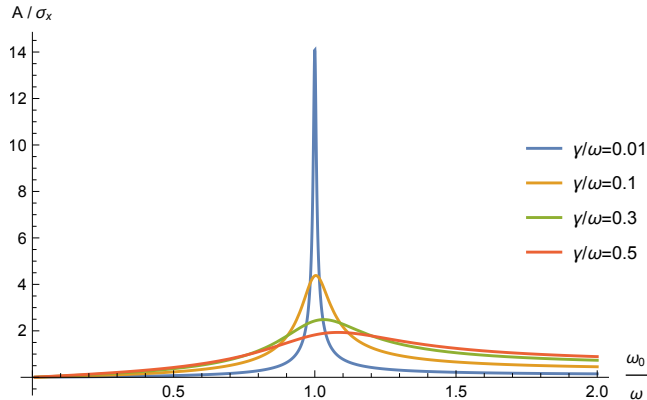


FIG. 9: The signal-to-noise  $A/\sigma_x$  of the harmonic oscillation as a function of  $\omega_0$  for different values of  $\gamma$ . Because the amplitude  $A$  exhibits a strong maximum at  $\omega_0 = \omega$ , the SNR peaks around  $\omega_0 = \omega$ . However, the maximum is not precisely at  $\omega_0 = \omega$ , because the noise  $\sigma_x$  peaks at  $\omega_0 = 0$  and not at  $\omega_0 = \omega$ . Depending on the friction, there thus exists an optimal intrinsic frequency  $\omega_0^{\text{opt}} > \omega$ . Note also that when  $\omega \neq \omega_0$ , it is actually beneficial to have friction,  $\gamma \neq 0$ .

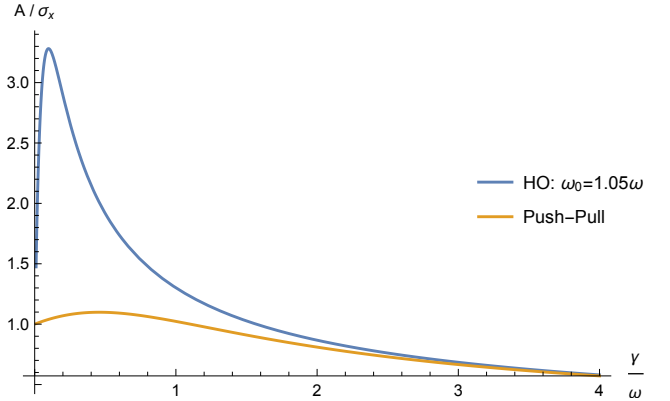


FIG. 10: The signal-to-noise  $A/\sigma_x$  as a function of  $\gamma$  for the harmonic oscillator and the push-pull network. For the harmonic oscillator, the friction is varied, while  $\omega_0$  is kept constant; for the push-pull network  $\mu$  is varied according to  $\mu = \omega_0^2/\gamma$ . It is seen that for low and intermediate friction the harmonic oscillator outperforms the push-pull network, but that in the high-friction limit they perform similarly.

the Stuart-Landau model, which provides a universal description of a weakly non-linear system near the Hopf bifurcation where a limit cycle appears. We use it to analyze the time-keeping properties of a system as it is altered from essentially a damped linear oscillator to a weakly non-linear oscillator, see Fig. 3 of the main text. Our treatment follows largely that of Pikovsky *et al.* [22].

### The amplitude equation

We consider the weakly non-linear oscillator [22]:

$$\ddot{x} + \omega_0^2 x = f(x, \dot{x}) + \rho s(t), \quad (67)$$

with  $s(t) = \sin(\omega t) + \bar{s} + \eta_s$  being the driving signal as before. The quantity  $f(x, \dot{x})$  describes the non-linearity of the autonomous oscillator and the parameter  $\rho$  controls

the strength of the forcing. The description presented below is valid in the regime where the non-linearity  $f(x, \dot{x})$  is small and the strength of the driving, quantified by  $\rho$ , is small. We begin by developing the formalism in the deterministic limit  $\eta_s = 0$ , in which  $s(t)$  is periodic with period  $T = 2\pi/\omega$ , before returning to the effects of noisy driving. In contrast to previous sections, our discussion here is limited to input noise that is not only Gaussian but white,  $\langle \eta_s(t) \rangle = 0$  and  $\langle \eta_s(t)\eta_s(t') \rangle = \sigma_s^2 \delta(t - t')$ .

Eq. 67 is close to that of a linear oscillator. We therefore expect that its solution has a nearly sinusoidal form. Moreover, we expect at least over some parameter range the frequency of the system is entrained by that of the driving signal. We therefore write the solution as

$$x(t) = \text{Re} [A(t)e^{i\omega t}] = \frac{1}{2} (A(t)e^{i\omega t} + \text{c.c.}), \quad (68)$$

where c.c. denotes complex conjugate. The above equation has the form of an harmonic oscillation with frequency  $\omega$ , but with a time-dependent complex amplitude  $A(t)$ . We emphasize that the observed frequency may deviate from  $\omega$ , when the amplitude  $A(t)$  rotates in the complex plane.

The above equation determines only the real part of the complex number  $A(t)e^{i\omega t}$ . To fully specify  $A(t)$ , we also need to set the imaginary part of  $A(t)e^{i\omega t}$ , which we choose to do via

$$y(t) = -\omega \text{Im} [A(t)e^{i\omega t}] = \frac{1}{2} (i\omega A(t)e^{i\omega t} + \text{c.c.}) \quad (69)$$

$$= \dot{x}. \quad (70)$$

The relation  $y(t) = \dot{x}$  thus specifies the imaginary part of the amplitude  $A(t)$ . Hence, the complex amplitude can be written as

$$A(t)e^{i\omega t} = x(t) - iy(t)/\omega. \quad (71)$$

Writing  $A(t) = R(t)e^{i\phi(t)}$ , it can be verified that

$$x(t) = R(t) \cos(\phi(t) + \omega t) \quad (72)$$

$$y(t) = -\omega R(t) \sin(\phi(t) + \omega t) \quad (73)$$

$$R^2(t) = x^2(t) + y^2(t)/\omega^2, \quad (74)$$

and that the specification  $\dot{x}(t) = y(t)$  implies that

$$\frac{\dot{R}(t)}{R(t)} = \dot{\phi}(t) \tan(\phi(t) + \omega t). \quad (75)$$

Eq. 73 shows that the time derivative of  $y(t)$  is

$$\begin{aligned} \dot{y} &= -\omega^2 x \\ &- \omega \left[ \dot{R}(t) \sin(\phi(t) + \omega t) + R(t) \dot{\phi}(t) \cos(\phi(t) + \omega t) \right] \end{aligned} \quad (76)$$

On the other hand, we know that

$$\begin{aligned} i\omega \dot{A}e^{i\omega t} &= -\omega \left[ \dot{R}(t) \sin(\phi(t) + \omega t) + R(t) \dot{\phi}(t) \cos(\phi(t) + \omega t) \right] \\ &+ i\omega \left[ \dot{R}(t) \cos(\phi(t) + \omega t) - R(t) \dot{\phi}(t) \sin(\phi(t) + \omega t) \right] \end{aligned} \quad (77)$$

$$= \dot{y} + \omega^2 x. \quad (78)$$

where in Eq. 77 we have exploited that the imaginary part is zero because of Eq. 75. Combing the above equation with Eq. 67, noting that  $\dot{y} = \ddot{x}$ , yields the following equation for the time evolution of the amplitude:

$$\dot{A} = \frac{e^{-i\omega t}}{i\omega} [(\omega^2 - \omega_0^2)x + f(x, y) + \rho s(t)]. \quad (79)$$

### Averaging

The above transformation is exact. To make progress, we will use the method of averaging [34]. Specifically, we will time average Eq. 79 over one period  $T$  [22, 34]. Averaging the driving  $e^{-i\omega t}s(t)/(i\omega)$  yields the complex constant  $E/(2\omega)$ . The second term of Eq. 79 can be expanded in polynomials of  $x(t) = (1/2)\text{Re}A(t)e^{i\omega t}$  and  $y(t) = (1/2)\text{Im}A(t)e^{i\omega t}$ , yielding powers of the type  $(A(t)e^{i\omega t})^n (A^*(t)e^{-i\omega t})^m$ . After multiplying with  $e^{-i\omega t}$  and averaging over one period  $T$ , only the terms with  $m = n - 1$  do not vanish. Consequently, the terms that remain after averaging have the form  $g(|A|^2)A$ , with an arbitrary function  $g$ . For small amplitudes only the linear term proportional to  $A$  and the first non-linear term,  $\propto |A|^2 A$  term are important. Finally, averaging the first term of Eq. 79 yields a term linear in  $A$ .

Summing it up, the time evolution of the amplitude of the system with deterministic driving ( $\eta_s = 0$ ) is given by [22]

$$\dot{A} = -i\frac{\omega^2 - \omega_0^2}{2\omega} A + \alpha A - (\beta + i\kappa)|A|^2 A - \frac{\rho}{2\omega} E \quad (80)$$

The parameters have a clear interpretation. The parameters  $\alpha$  and  $\beta$  describe, respectively, the linear and non-linear growth or decay of oscillations. To have stable oscillations, both in the presence and absence of driving, large amplitude oscillations dominated by the nonlinear term need to decay, which means that  $\beta$  must be positive,  $\beta > 0$ ; this parameter is fixed in all our calculations. The parameter that allows us to alter the system from one that shows damped oscillations in the absence of driving to one that can generate autonomous oscillations which do not rely on forcing, is  $\alpha$ . For the system to sustain free-running oscillations, small amplitude oscillations, dominated by the linear term, must grow, meaning that  $\alpha$  must be positive,  $\alpha > 0$ . The case with  $\alpha > 0$  thus describes a system that can perform stable limit cycle oscillations, making it a bonafide clock. The case

$\alpha < 0$  describes a system that in the absence of any driving,  $E = 0$ , relaxes in an oscillatory fashion to a stable fixed point with  $A = 0$ . In the presence of weak driving, the amplitude  $A$  at the fixed point will be non-zero but small, making the effect of the non-linearity weak. The case  $\alpha < 0$  thus describes a system that is effectively a damped harmonic oscillator, which only displays sustained oscillations when forced by an oscillatory signal. This system mimics the uncoupled-hexamer model.

The parameter  $\kappa$  describes the non-linear dependence of the oscillation frequency on the amplitude. For the isochronous scenario in which the phase moves with a constant velocity,  $\kappa = 0$ , which is what we will assume henceforth.

Defining the parameter  $\nu \equiv (\omega^2 - \omega_0^2)/(2\omega)$  and the parameter  $\epsilon \equiv \rho/(2\omega)$ , we can then rewrite the above equation as

$$\dot{A} = -i\nu A + \alpha A - \beta|A|^2 A - \epsilon E, \quad (81)$$

where  $A$  is the complex time-dependent amplitude,  $E$  is a complex constant, and  $\nu$ ,  $\alpha$ , and  $\beta$  are real constants. Eq. 81 is Eq. 2 of the main text. It provides a universal description of a driven weakly nonlinear system near the Hopf bifurcation where the limit cycle appears [22].

To model the input noise we will add the noise term to Eq. 81:

$$\dot{A} = -i\nu A + \alpha A - \beta|A|^2 A - \epsilon E + \rho\bar{\eta}_s(t), \quad (82)$$

where  $\bar{\eta}_s(t)$  is the noise  $\eta_s(t)$  averaged over one period of the driving:

$$\bar{\eta}_s(t) \equiv \frac{1}{T} \int_{t-T/2}^{t+T/2} dt' \frac{e^{-i\omega t'}}{i\omega} \eta_s(t'). \quad (83)$$

Since  $\eta_s(t)$  is real but its prefactor  $e^{-i\omega t}/i\omega$  is complex,  $\bar{\eta}_s(t)$  is, in general, complex. Below we will describe the characteristics of the noise  $\bar{\eta}_s$ .

#### Linear-Noise Approximation

**Scenarios** By varying  $\alpha$  we will interpolate between two scenarios: the damped oscillator, modeling the UHM, with  $\alpha < 0$ , and the weakly non-linear oscillator that can sustain free-running oscillations, modeling the CHM, with  $\alpha > 0$ . For the system with  $\alpha < 0$ , the amplitude of  $x(t)$  when not driven is  $A = 0$ : the system comes to a standstill. When the system is driven, the amplitude will be nonzero, but constant since the system is essentially linear as described above. For the system with  $\alpha > 0$ ,  $A(t)$  can exhibit distinct types of dynamics, depending on the strength of driving and the frequency mismatch characterized by  $\nu$  [22]. However, here we do not consider the regimes that  $A(t)$  rotates in the complex plane; we will limit ourselves to the scenario

that  $A(t) = A$  is constant, meaning that  $\nu$  cannot be too large [22].

**Overview** Before we discuss the linear-noise approximation in detail, we first give an overview. The central observation is that both for the driven damped oscillator with  $\alpha < 0$  and the driven limit-cycle oscillator with  $\alpha > 0$ , the complex amplitude  $A$  is constant, corresponding to a stable fixed point of the amplitude equation, Eq. 81. In the spirit of the linear-noise approximation used to calculate noise in biochemical networks, we then expand around the fixed point to linear order, and evaluate the noise at the fixed point. This approach thus assumes that the distribution of the variables of interest is Gaussian, centered at the fixed point. More concretely, we first expand  $A(t)$  to linear order around its stable fixed point, which is obtained by setting  $\dot{A}$  in Eq. 81 to zero. This makes it possible to compute the variance of  $A$ . Importantly, this variance is that of a Gaussian distribution in the frame that co-rotates with the driving, as can be seen from Eqs. 72 and 73. To obtain the variance of  $x$  and  $y$  in the original frame, we then transform this distribution back to original frame of  $x$  and  $y$ . If we can make this transformation linear, then it is guaranteed that the distribution of  $x$  and  $y$  will also be Gaussian. As we will see, the transformation can be made linear by writing  $A$  as  $A = u + iv$ , where  $u$  and  $v$  are the real and imaginary parts of  $A$ , respectively.

**Expanding  $A$  around its fixed point** We write  $A(t) = u(t) + iv(t)$ . Eq. 82 then yields for the real and imaginary part of  $a(t)$ :

$$\dot{u} = \nu u + \alpha u - \beta(u^2 + v^2)u - \epsilon e_u + \rho\bar{\eta}_u \quad (84)$$

$$\dot{v} = -\nu v + \alpha v - \beta(u^2 + v^2)v - \epsilon e_v + \rho\bar{\eta}_v \quad (85)$$

Here,  $\bar{\eta}_u$  and  $\bar{\eta}_v$  are the real and imaginary parts of the averaged noise  $\bar{\eta}_s$ , given by Eq. 83; they are discussed below. The quantities  $e_u$  and  $e_v$  are the real and imaginary parts of the driving  $E$ . Their respective values depend on the phase of the driving, which is arbitrary and can be chosen freely. For example, when the driving is  $s(t) = \sin(\omega t)$ , then  $e_u = 1$  and  $e_v = 0$ , while if the signal is  $s(t) = \cos(\omega t)$ , then  $e_u = 0$  and  $e_v = 1$ .

We now expand  $u(t)$  and  $v(t)$  around their steady-state values,  $u^*$  and  $v^*$ , respectively. Inserting this in the above equations and expanding up to linear order yields

$$\delta\dot{u} = c_1\delta u + c_2\delta v + \rho\bar{\eta}_u \quad (86)$$

$$\delta\dot{v} = c_3\delta u + c_4\delta v + \rho\bar{\eta}_v, \quad (87)$$

with

$$c_1 = \alpha - \beta(3u^{*2} + v^{*2}) \quad (88)$$

$$c_2 = \nu - \beta 2u^*v^* \quad (89)$$

$$c_3 = -\nu - \beta 2u^*v^* \quad (90)$$

$$c_4 = \alpha - \beta(u^{*2} + 3v^{*2}). \quad (91)$$

The fixed points  $u^*$  and  $v^*$  are obtained by solving the cubic equations Eqs. 84 and 85 in steady state.

**Noise characteristics** We next have to specify the noise characteristics of  $\bar{\eta}_u(t)$  and  $\bar{\eta}_v(t)$ . Eq. 83 reveals that the noise terms are given by

$$\bar{\eta}_u(t) = -\frac{1}{\omega T} \int_{t-T/2}^{t+T/2} dt' \sin(\omega t') \eta_s(t') \quad (92)$$

$$\bar{\eta}_v(t) = -\frac{1}{\omega T} \int_{t-T/2}^{t+T/2} dt' \cos(\omega t') \eta_s(t'). \quad (93)$$

The method of averaging [35] reveals that to leading order the statistics of these quantities can be approximated by

$$\langle \bar{\eta}_u(t) \bar{\eta}_u(t') \rangle = \langle \bar{\eta}_v(t) \bar{\eta}_v(t') \rangle = \frac{\sigma_s^2}{2\omega^2} \delta(t-t') \quad (94)$$

$$\langle \bar{\eta}_u(t) \bar{\eta}_v(t') \rangle = 0. \quad (95)$$

**Variance-co-variance** From here, there are (at least) three ways to obtain the variance and co-variance matrix of  $u$  and  $v$ . Since the system is linear, it can be directly solved in the time domain. Another route is via the power spectra [30, 36]. Here, we obtain it from [37]

$$\mathbf{A} \mathbf{C}_{uv} + \mathbf{C}_{uv} \mathbf{A}^T = -\mathbf{D}_{uv}. \quad (96)$$

The matrix  $\mathbf{C}_{uv}$  is the variance-covariance matrix with elements  $\sigma_{uu}^2, \sigma_{uv}^2, \sigma_{vu}^2, \sigma_{vv}^2$  and  $\mathbf{A}$  is the Jacobian of Eqs. 86 and 87 with elements  $A_{11} = c_1, A_{12} = c_2, A_{21} = c_3, A_{22} = c_4$ . The matrix  $\mathbf{D}_{uv}$  is the noise matrix of  $\langle \bar{\eta}_{u/v}^2 \rangle$ , where we absorb the coupling strength  $\rho = 2\omega\epsilon$  (cf. Eq. 81) in the noise strength:

$$\mathbf{D}_{uv} = \begin{pmatrix} 2\epsilon^2 \sigma_s^2 & 0 \\ 0 & 2\epsilon^2 \sigma_s^2 \end{pmatrix}. \quad (97)$$

**Transforming back** The variance-covariance matrix  $\mathbf{C}_{uv}$ , with elements  $\sigma_{uu}^2, \sigma_{uv}^2, \sigma_{vu}^2, \sigma_{vv}^2$ , characterizes a Gaussian distribution in the complex plane

$$P(u, v) = \frac{1}{2\pi \sqrt{|\mathbf{C}_{uv}|}} e^{-\frac{1}{2} \mathbf{a}^T \mathbf{C}_{uv}^{-1} \mathbf{a}}, \quad (98)$$

where  $|\mathbf{C}_{uv}|$  is the determinant of the variance-covariance matrix  $\mathbf{C}_{uv}$  and  $\mathbf{C}_{uv}^{-1}$  is the inverse of  $\mathbf{C}_{uv}$ , and  $\mathbf{a}$  is a vector with elements  $\delta u, \delta v$  (the deviations of the real and imaginary parts of  $A = a$  from their respective fixed points  $u^*$  and  $v^*$ ) with  $\mathbf{a}^T$  its transpose. This distribution  $P(u, v)$  defines a distribution in the co-rotating frame of the oscillator in the complex plane. To obtain  $P(x, y)$  in the original non-co-rotating frame, we need to rotate this distribution. Eq. 71 shows that the corresponding rotation is described by

$$x(t) = u \cos(\omega t) - v \sin(\omega t) \quad (99)$$

$$y(t) = -\omega u \sin(\omega t) - \omega v \cos(\omega t), \quad (100)$$

which defines the rotation matrix

$$\mathbf{Q} = \begin{pmatrix} \cos(\omega t) & -\sin(\omega t) \\ -\omega \sin(\omega t) & -\omega \cos(\omega t) \end{pmatrix} \quad (101)$$

such that  $\mathbf{z} = \mathbf{Q} \mathbf{a}$ , with  $\mathbf{z}$  the vector with elements  $\delta x(t) = x(t) - x^*(t), \delta y(t) = y(t) - y^*(t)$ , where  $x^*, y^*$  are the rotating ‘‘fixed’’ points of  $x(t)$  and  $y(t)$ , i.e. their time-dependent mean values, given by Eqs. 99 and 100 with  $u = u^*$  and  $v = v^*$ . Hence, the distribution of interest is given by

$$P(x, y|t) = \frac{1}{2\pi \sqrt{|\mathbf{C}_{xy}|}} e^{-\frac{1}{2} \mathbf{z}^T \mathbf{C}_{xy}^{-1} \mathbf{z}}, \quad (102)$$

where

$$\mathbf{C}_{xy}^{-1} = [\mathbf{Q}^{-1}]^T \mathbf{C}_{uv}^{-1} \mathbf{Q}^{-1} \quad (103)$$

and its inverse  $\mathbf{C}_{xy}$  is the variance-covariance matrix for  $x, y$ , with elements  $\sigma_{xx}^2(t), \sigma_{xy}^2(t), \sigma_{yx}^2(t), \sigma_{yy}^2(t)$ , which depend on time because  $\mathbf{Q}$  depends on time.

**Mutual information**  $I(p; t)$  Lastly, the oscillations in the phosphorylation  $p(t)$  of the hexamer models correspond to the oscillations in  $x(t)$  in the Stuart-Landau model. We therefore need to compute the mutual information  $I(x; t)$ , not  $I(x, y; t)$ . Specifically, we calculate the mutual information from

$$I(x, t) = H(x) - \langle H(x|t) \rangle_t, \quad (104)$$

where the entropy  $H(x) = -\int dx P(x) \log P(x)$  with  $P(x) = 1/T \int_0^T dt P(x|t)$  and the conditional entropy  $H(x|t) = -1/T \int_0^T dt \int dx P(x|t) \log P(x|t)$ , with  $P(x|t) = 1/\sqrt{2\pi\sigma_{xx}^2(t)} e^{-(x(t)-x^*(t))^2/(2\sigma_{xx}^2(t))}$ . We emphasize that both the variance  $\sigma_{xx}^2(t)$  and the average  $x^*(t)$  depend on time.

**Summing up Approach and Parameters** **Fig. 3 main text** To sum up the procedure, to compute the noise in  $A = a$  we first need to obtain the steady state values of its real and imaginary part,  $\bar{u}$  and  $\bar{v}$  (see Eqs. 88-91). These are obtained from setting the time derivatives of  $u(t)$  and  $v(t)$  in Eqs. 84 and 85 to zero; this involves solving a cubic equation, which we do numerically. We then compute the variance-covariance matrix  $\mathbf{C}_{uv}$  via Eq. 96, where the elements of the Jacobian  $\mathbf{A}$  are given by Eqs. 88-91 and the noise matrix  $\mathbf{D}_{uv}$  is given by Eq. 97. After having obtained  $\mathbf{C}_{uv}$ , we find the variance-covariance matrix for  $x$  and  $y$ ,  $\mathbf{C}_{xy}$ , from Eq. 103. For Fig. 3 of the main text,  $\nu = 0, \beta = \omega, \epsilon = 0.5\omega$ .

*Comparing limit cycle oscillator with damped oscillator*

Fig. 3 of the main text shows that the mutual information  $I(x; t)$  increases with  $\alpha$ , especially when the input noise is large. To elucidate this further, we show

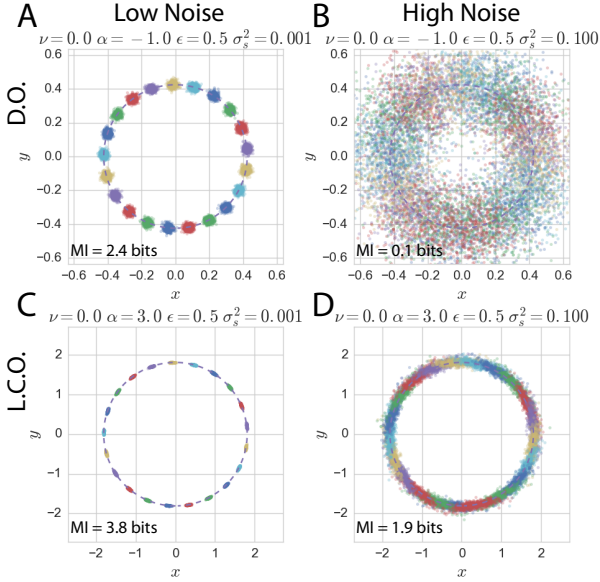


FIG. 11: The dynamics of the Stuart-Landau model when  $\alpha = -\omega$ , corresponding to a damped oscillator (D.O., top row), and when  $\alpha = 3\omega$ , corresponding to a limit-cycle oscillator (L.C.O., bottom row), both for low input noise,  $\sigma_s^2 = 0.001$  (left column) and high input noise,  $\sigma_s^2 = 0.1$  (right column). Dashed line denotes the mean trajectory of  $(x, y)$ , and the points are samples of  $(x, y)$  from the distribution  $P(x, y|t_i)$  for evenly spaced time points  $t_i$ ;  $P(x, y|t)$  is given by Eq. 102 and points belonging to the same time have the same color. It is seen that when the input noise is low, the distributions corresponding to the different times are still well separated, both for the limit-cycle oscillator and the damped oscillator. Yet, for high noise, only for the L.C.O. are the distributions still reasonably separated, leading to a mutual information that is still close to 2 bits. In contrast, for the D.O., the distributions are mixed, leading to a low mutual information close to zero.

in Fig. 11 for two different values of  $\alpha$  and for two levels of the input noise, the dynamics of the system in the plane of  $x$  and  $y$ . The panels not only show the mean trajectory, indicated by the dashed line, but also samples  $(x, y)$  from  $P(x, y|t_i)$  for evenly spaced time points  $t_i$ ;  $P(x, y|t)$  is given by Eq. 102 and samples from the same time point  $t_i$  have the same color. It is seen that when the input noise is low (left two panels), the respective distributions (“blobs”) are well separated, both for  $\alpha = -\omega$ , when the system is a damped oscillator (D.O.) (top row), and for  $\alpha = 3\omega$  (bottom row), when the system is a limit-cycle oscillator (L.C.O.). However, when the input noise is large (right column), the blobs of the damped oscillator become mixed, while the distributions  $P(x, y|t)$  of the limit-cycle oscillator are still fairly well separated.

To interpret this further, we note that the mutual information  $I(x; t) = H(t) - H(t|x)$ . Here,  $H(t)$  is the entropy of the input signal, which is constant,

i.e. does not depend on the design of the system. The dependence of  $I(x; t)$  on the design of the system is thus governed by the conditional entropy, given by  $H(t|x) = \langle \langle -\log P(t|x) \rangle_{P(t|x)} \rangle_{P(x)}$ . The quantity  $\langle -\log P(t|x) \rangle_{P(t|x)}$  quantifies the uncertainty in estimating the time  $t$  from a given output  $x$ ; the average  $\langle \dots \rangle_{P(x)}$  indicates that this uncertainty should be averaged over all output values  $x$  weighted by  $P(x)$ . The conditional entropy  $H(t|x)$  is low and  $I(x; t)$  is high when, averaged over  $x$ , the distribution  $P(t|x)$  of times  $t$  for a given  $x$  is narrow. We can now interpret Fig. 11: The smaller the number of blobs that intersect the line  $x$ , the higher the mutual information. Or, concomitantly, the more the distributions are separated, the higher the mutual information—information transmission is indeed a packing problem. Clearly, when the input noise is low, the time can be inferred reliably from the output even with a damped oscillator (top left panel). For high input noise, however, the mutual information of the damped oscillator falls dramatically because the blobs now overlap strongly. In contrast, the distributions of the limit-cycle oscillator are still reasonably separated and  $I(x; t)$  is still almost close to 2 bits.

Fig. 11 also nicely illustrates that the mutual information would be increased if the system could estimate the time not from  $x$  only, but instead from  $x$  and  $y$ : this removes the degeneracy in estimating  $t$  for a given  $x$  associated with sinusoidal oscillations [19]. One mechanism to remove the degeneracy is to have a readout system that not only reads out the amplitude of the clock signal, but also its derivative, for example via incoherent feedback loops [21]. Another possibility is that the clock signal is read out by 2 (or more) proteins that are out of phase with each other, as shown in [19]. Indeed, while we have computed the instantaneous mutual information between time and the output at a given time, the trajectory of the clock signal provides more information about time, which could in principle be extracted by appropriate readout systems [19].

Lastly, we show in Fig. 12 the dynamics for two different values of  $\alpha$  and for two different values of the coupling strength  $\epsilon$ . The top left panel shows that when  $\epsilon$  is small, the amplitude of the damped oscillator is very weak—note the scale on the  $x$ - and  $y$ -axis. To increase the amplitude of the output, the coupling strength must be increased. However, this amplifies the input noise as well, such that the mutual information remains unchanged (top right panel): the damped oscillator faces a fundamental trade-off between gain and input noise that cannot be lifted. In contrast, the limit-cycle oscillator (bottom row) already exhibits strong amplitude oscillations even when the coupling strength  $\epsilon$  is small: the amplitude of the cycle—a bonafide limit-cycle—is determined by the properties of the system, and is only very weakly affected by the strength of the forcing. Moreover, Figs. 11 and 12 show that while the fluctuations in the

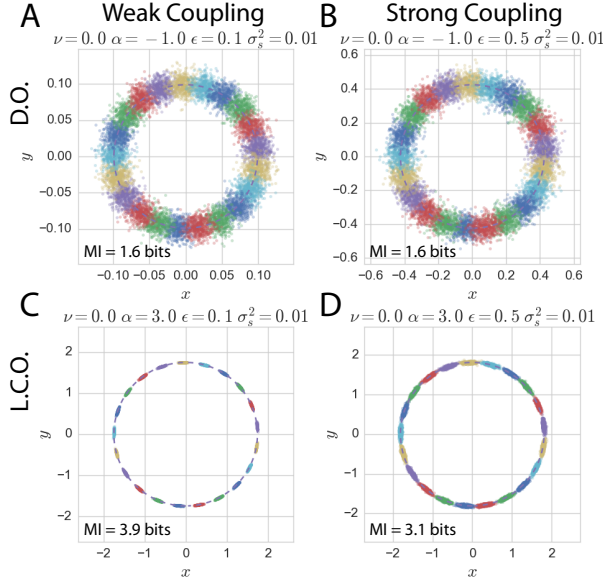


FIG. 12: The dynamics of the Stuart-Landau model when  $\alpha = -\omega$ , corresponding to a damped oscillator (D.O., top row), and when  $\alpha = 3\omega$ , corresponding to a limit-cycle oscillator (L.C.O., bottom row), both for weak coupling,  $\epsilon = 0.1\omega$  (left column) and strong coupling,  $\epsilon = 0.5\omega$  (right column). Dashed line denotes the mean trajectory of  $(x, y)$ , and the points are samples of  $(x, y)$  from the distribution  $P(x, y|t_i)$  for evenly spaced times  $t_i$ ;  $P(x, y|t)$  is given by Eq. 102 and points belonging to the same time have the same color. It is seen that for the D.O. the amplitude and the noise are small when the coupling is small (top left panel; note the scale on the x- and y-axis). Increasing the coupling, however, not only raises the amplitude, but also amplifies the noise, leaving the mutual information unchanged: a damped oscillator cannot lift the trade-off between gain and noise. In contrast, the limit-cycle oscillator already exhibits large amplitude oscillations even for weak coupling. Especially the fluctuations in the radial direction, the amplitude fluctuations, are strongly reduced in the L.C.O., due to the non-linearity of the system.

phase are not significantly smaller for the limit-cycle oscillator than for the damped oscillator, the relative fluctuations in the amplitude (compared to the mean) are much smaller for the limit-cycle oscillator, due to the non-linearity of the confining potential.

#### Optimal intrinsic frequency

Fig. 6B shows that the optimal intrinsic frequency  $\omega_0^{\text{opt}}$  that maximizes the mutual information  $I(p; t)$  for the coupled-hexamer model (CHM) depends, albeit very weakly, on the input-noise strength  $\sigma_s^2$ . Here we wondered whether the Stuart-Landau model could reproduce this feature. Fig. 13 shows the result. The figure shows the mutual information  $I(x; t)$  as a function

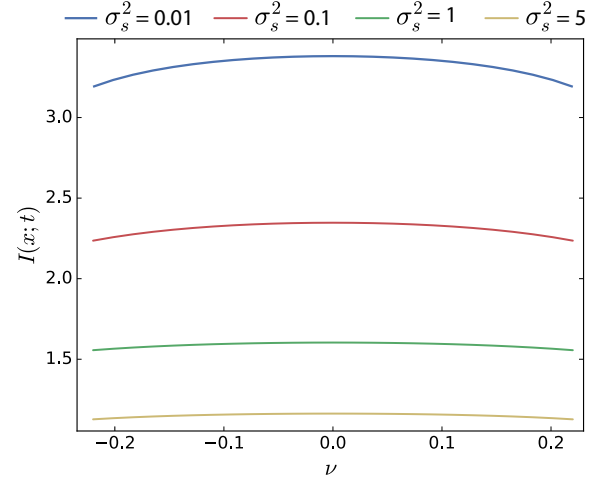


FIG. 13: The mutual information  $I(x; t)$  in the Stuart-Landau model as a function of  $\nu = (\omega^2 - \omega_0^2)/(2\omega)$ , for different input-noise strengths  $\sigma_s^2$ . It is seen that the mutual information is maximized at  $\nu = 0$  (corresponding to  $\omega_0 = \omega$ ) for all input noise levels.  $\beta = 1.0\omega$ ;  $\epsilon = 0.5\omega$ ;  $\alpha = 3\omega$ .

of  $\nu = (\omega^2 - \omega_0^2)/(2\omega)$  for different values of  $\sigma_s^2$ . It is seen that the dependence of  $I(x; t)$  on  $\nu$  is rather weak, yielding a broad maximum that peaks at  $\nu = 0$  (corresponding to  $\omega_0 = \omega$ ) for all noise strengths. This suggests that the optimal  $\omega_0^{\text{opt}} < \omega$  observed for low input noise in the CHM arises from a stronger non-linearity in that system than captured by the Stuart-Landau model, which describes weakly non-linear oscillators.

- [1] T. Roenneberg and M. Merrow, *Journal of Biological Rhythms* **17**, 495 (2002).
- [2] P. Ma *et al.*, *PLoS genetics* **12**, e1005922 (2016).
- [3] M. Ishiura *et al.*, *Science* **281**, 1519 (1998).
- [4] M. Nakajima *et al.*, *Science (New York, N.Y.)* **308**, 414 (2005).
- [5] J. Holtzendorff *et al.*, *Journal of Biological Rhythms* **23**, 187 (2008).
- [6] E. R. Zinser *et al.*, *PLoS ONE* **4**, e5135 (2009).
- [7] C. Troein, J. C. W. Locke, M. S. Turner, and A. J. Millar, *Current Biology* **19**, 1961 (2009).
- [8] M. J. Rust, S. S. Golden, and E. K. O'Shea, *Science (New York, N.Y.)* **331**, 220 (2011).
- [9] G. K. Pattanayak, G. Lambert, K. Bernat, and M. J. Rust, *Cell Reports* **13**, 2362 (2015).
- [10] M. Monti, D. K. Lubensky, and P. R. ten Wolde, *arXiv.org:1706.02226* (2017).
- [11] J. S. van Zon, D. K. Lubensky, P. R. H. Altena, and P. R. ten Wolde, *Proc Natl Acad Sci USA* **104**, 7420 (2007).
- [12] M. J. Rust *et al.*, *Science* **318**, 809 (2007).
- [13] S. Clodong *et al.*, *Molecular Systems Biology* **3**, 90 (2007).
- [14] T. Mori *et al.*, *PLoS Biology* **5**, e93 (2007).
- [15] D. Zwicker, D. K. Lubensky, and P. R. ten Wolde, *Pro-*

- ceedings of the National Academy of Sciences of the United States of America **107**, 22540 (2010).
- [16] J. Lin, J. Chew, U. Chockanathan, and M. J. Rust, Proceedings of the National Academy of Sciences of the United States of America **111**, E3937 (2014).
- [17] J. Paijmans, D. K. Lubensky, and P. R. ten Wolde, PLoS Computational Biology **13**, e1005415 (2017).
- [18] J. Paijmans, D. K. Lubensky, and P. R. ten Wolde, Biophys. J. **113**, 157 (2017).
- [19] M. Monti and P. R. ten Wolde, Physical Biology **13**, 1 (2016).
- [20] Supporting Information.
- [21] N. B. Becker, A. Mugler, and P. R. ten Wolde, Physical Review Letters **115**, 258103 (2015).
- [22] A. Pikovsky, M. Rosenblum, and J. Kurths, *Synchronization: A universal concept in nonlinear sciences* (Cambridge University Press, Cambridge, 2003).
- [23] Y. Xu, T. Mori, and C. H. Johnson, The EMBO journal **19**, 3349 (2000).
- [24] Y. Nakahira *et al.*, Proceedings of the National Academy of Sciences of the United States of America **101**, 881 (2004).
- [25] T. Nishiwaki *et al.*, Proceedings of the National Academy of Sciences **101**, 13927 (2004).
- [26] J. Tomita, M. Nakajima, T. Kondo, and H. Iwasaki, Science **307**, 251 (2005).
- [27] S. W. Teng *et al.*, Science **340**, 737 (2013).
- [28] J. Paijmans, M. Bosman, P. R. ten Wolde, and D. K. Lubensky, Proceedings of the National Academy of Sciences of the United States of America **113**, 4063 (2016).
- [29] J. Paulsson, Nature **427**, 415 (2004).
- [30] S. Tănase-Nicola, P. B. Warren, and P. R. ten Wolde, Physical Review Letters **97**, 068102 (2006).
- [31] C. C. Govern and P. R. ten Wolde, Physical Review Letters **113**, 258102 (2014).
- [32] R. Cheong *et al.*, Science **334**, 354 (2011).
- [33] F. Tostevin and P. R. ten Wolde, Physical Review E **81**, 061917 (2010).
- [34] J. Guckenheimer and P. J. Holmes, *Nonlinear Oscillations, Dynamical Systems, and Bifurcations of Vector Fields* (Springer, New York, ADDRESS, 1983).
- [35] V. S. Anishchenko *et al.*, Nonlinear dynamics of chaotic and stochastic systems: tutorial and modern developments (2007).
- [36] P. B. Warren, S. Tănase-Nicola, and P. R. ten Wolde, The Journal of Chemical Physics **125**, 144904 (2006).
- [37] C. W. Gardiner, *Handbook of Stochastic Methods* (Springer-Verlag, Berlin, 1985).